JACS
JOURNAL OF THE AMERICAN CHEMICAL SOCIETY
Article
pubs.acs.org/JACS

# $Rh_2$(II,III) Catalysts with Chelating Carboxylate and Carboxamidate Supports: Electronic Structure and Nitrene Transfer Reactivity

Adrián Varela-Álvarez,[†,⊥] Tzuhsiung Yang,[‡,⊥] Heather Jennings,[‡] Katherine P. Kornecki,[‡] Samantha N. Macmillan,[§] Kyle M. Lancaster,[§] James B. C. Mack,[∥] J. Du Bois,[∥] John F. Berry,*[,‡] and Djamaladdin G. Musaev*[,†]

[†]The Cherry L. Emerson Center for Scientific Computation, Emory University, 1515 Dickey Drive, Atlanta, Georgia 30322, United States

[‡]Department of Chemistry, University of Wisconsin—Madison, 1101 University Avenue, Madison, Wisconsin 53706, United States

[§]Department of Chemistry and Chemical Biology, Cornell University, Ithaca, New York 14853, United States

[∥]Department of Chemistry, Stanford University, Stanford, California 94305, United States

Supporting Information

**ABSTRACT:** Dirhodium-catalyzed C−H amination is hypothesized to proceed via $Rh_2$-nitrene intermediates in either the $Rh_2$(II,II) or $Rh_2$(II,III) redox state. Herein, we report joint theoretical and experimental studies of the ground electronic state (GES), redox potentials, and C−H amination of $[Rh_2^{II,III}(O_2CCH_3)_4(L)_n]^+$ (**1_L**) (**L** = none, $Cl^-$, and $H_2O$), $[Rh_2(esp)_2]^+$ (**2**), and $Rh_2(espn)_2Cl$ (**3**) (esp = $\alpha,\alpha,\alpha',\alpha'$-tetramethyl-1,3-benzenedipropanoate and espn = $\alpha,\alpha,\alpha',\alpha'$-tetramethyl-1,3-benzenedipropanamidate). CASSCF calculations on **1_L** yield a wave function with two closely weighted configurations, $(\delta^*)^2(\pi_1^*)^2(\pi_2^*)^1$ and $(\delta^*)^2(\pi_1^*)^1(\pi_2^*)^2$, consistent with reported EPR $g$ values [*Chem. Phys. Lett.* **1986**, *130*, 20−23]. In contrast, EPR spectra of **2** show $g$ values consistent with the DFT-computed $(\pi^*)^4(\delta^*)^1$ GES. EPR spectra and Cl K-edge XAS for **3** are consistent with a $(\pi^*)^4(\delta^*)^1$ GES, as supported by DFT. Nitrene intermediates **2N_L** and **3N_L** are also examined by DFT (the nitrene is an $NSO_3R$ species). DFT calculations suggest a doublet GES for **2N_L** and a quartet GES for **3N_L**. CASSCF calculations describe the GES of **2N** as $Rh_2$(II,II) with a coordinated nitrene radical cation, $(\pi^*)^4(\delta^*)^2(\pi_{nitrene,1})^1(\pi_{nitrene,2})^0$. Conversely, the GES of **3N** is $Rh_2$(II,III) with a coordinated triplet nitrene, $(\pi^*)^4(\delta^*)^1(\pi_{nitrene,1})^1(\pi_{nitrene,2})^1$. Quartet transition states ($^4$TSs) are found to react via a stepwise radical mechanism, whereas $^2$TSs are found to react via a concerted mechanism that is lower in energy compared to $^4$TSs for both **2N_L** and **3N_L**. The experimental (determined by intramolecular competition) and $^2$TS-calculated kinetic isotopic effect (KIE) shows a KIE ∼ 3 for both **2N** and **3N**, which is consistent with a concerted mechanism.

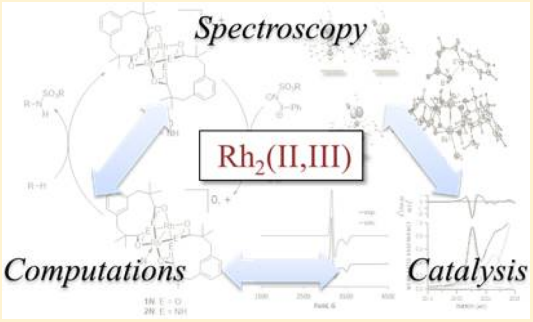


## 1. INTRODUCTION

C−H amination via nitrene transfer catalysis (NTC) has the potential to be a transformative method in synthetic organic chemistry.[1−5] Some of the leading catalysts for intra- and intermolecular C−H amination via NTC are coordination complexes with a Rh(II)−Rh(II) bond (Scheme 1), such as the $Rh_2$-tetracarboxylates and the $Rh_2(esp)_2$ (esp = $\alpha,\alpha,\alpha',\alpha'$-tetramethyl-1,3-benzenedipropanoate) catalyst bearing chelating dicarboxylate ligands, which operate best with sulfamate-derived nitrene species ($NSO_3R$).[6] Other catalysts such as silver,[7−11] iron,[12−18] manganese,[13,19,20] ruthenium,[19,21−23] copper,[24−30] and cobalt[31−34] complexes have been shown to perform C−H amination, as well. The $Rh_2$(II,II) complexes were initially presumed to perform C−H amination via a nitrene interception/insertion mechanism, as shown in Scheme 1,[6,35] in analogy to related carbene transfer reactions.[36] However, subsequently, Du Bois and Berry have independently shown the formation of mixed-valent $Rh_2$(II,III) species (including a $Rh_2$(II,III)-nitrene species proposed by Du Bois and Zare) under the highly oxidative NTC conditions, which are also believed to be active in NTC reactivity.[37−39]

Recently, the Berry group reported a new amidate-ligated $Rh_2$(II,III) catalyst, $Rh_2(espn)_2Cl$ (espn = $\alpha,\alpha,\alpha',\alpha'$-tetramethyl-1,3-benzenedipropanamidate), which is capable of performing intramolecular C−H amination and has a long lifetime under NTC conditions, achieving turnover numbers higher than those of $Rh_2(esp)_2$ by a factor of 3 in head-to-head intramolecular competition experiments.[40] The longer lifetime of $Rh_2(espn)_2Cl$ during NTC compared to that of $Rh_2(esp)_2$ may be attributed to the greater thermodynamic stability of the former complex. As has been well-documented, amidate ligands not only bind more strongly to the $Rh_2$ core than do

**Received:** December 16, 2015
**Published:** January 28, 2016




DOI: 10.1021/jacs.5b12790
J. Am. Chem. Soc. 2016, 138, 2327−2341

**Scheme 1. NTC Cycle for $Rh_2(esp)_2$ and $Rh_2(espn)_2Cl$**

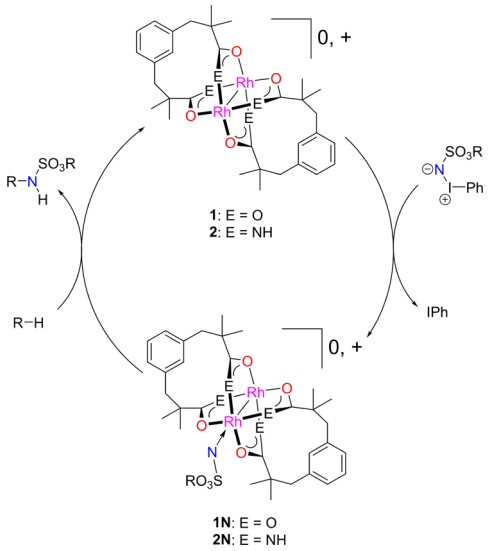


carboxylate ligands but also lower the potential required for oxidation of $Rh_2$(II,II) to the $Rh_2$(II,III) level.[41]

Compared to $Rh_2$(II,II) compounds, there are far fewer investigations of $Rh_2$(II,III) species. The most extensive electronic structure study of $Rh_2$(II,III) species, done by Norman and co-workers in 1979,[42] was very thorough but utilized methods that are now out of date and known to lead to inaccurate conclusions. The electronic structure of $Rh_2$(II,III) species is complex because of the existence of multiple low-lying electronic configurations, which could contribute to their total ground state wave function. $Rh_2$(II,II) complexes have a single Rh–Rh bond by virtue of the $(\sigma)^2(\pi)^4(\delta)^2(\delta^*)^2(\pi^*)^4$ electron configuration, where all Rh–Rh bonding and antibonding orbitals are filled with the exception of the $\sigma^*$ antibonding orbital.[43] The $\pi^*$ and $\delta^*$ orbitals located below the $\sigma^*$ orbital are very close in energy,[44] and thus, upon oxidation of $Rh_2$(II,II) to $Rh_2$(II,III), it is a priori unclear whether a $\pi^*$ or $\delta^*$ electron would be removed, leading, in rigorous $D_{4h}$ symmetry, to a $^2E_g$ or $^2B_{1u}$ ground electronic state (GES), respectively (Chart 1).

**Chart 1. Possible Ground States of $Rh_2$(II,III) Compounds**

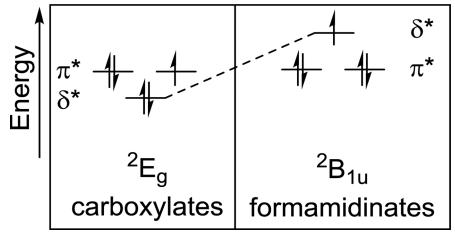


In principle, the $^2E_g$ and $^2B_{1u}$ states may be distinguished by EPR spectroscopy since the first-order spin–orbit coupling of the former state leads to the appearance of unusual EPR signals, with $g$ values widely different from the free electron value.[45] In this way, Kawamura and co-workers have shown that a range of $Rh_2$(II,III) carboxylate (O,O donor) complexes have the $^2E_g$ ground state, whereas $Rh_2$(II,III) compounds with N,N donor ligands (e.g., formamidinates) have the $^2B_{1u}$ ground state.[46−49] An interesting question arises in considering $Rh_2$(II,III) complexes with amidate (N,O donor) ligands: will these compounds have a $^2E_g$ ground state like the corresponding carboxylate compounds, or is the $\pi$-donation of the equatorial ligand field now strong enough that the $\delta^*$ orbital is raised above the $\pi^*$, leading to a $^2B_{1u}$ ground state like in the corresponding formamidinate compounds? An acetamidate-supported $Rh_2$(II,III) complex has been characterized by EPR spectroscopy in acetonitrile and DMSO solution and was found to have $g$ values, $g_\perp \sim 2.1$ and $g_\parallel \sim 1.9$, consistent with a single Kramer's doublet and therefore indicative of a $^2B_{1u}$-type $(\delta^*)^1$ ground state.[50]

Here we address the $Rh_2$(II,III) GES of $[Rh_2(OAc)_4(L)_n]^{m+}$, **1_(L)$_n$**, $[Rh_2(esp)_2(L)_n]^{m+}$, **2_(L)$_n$**, and $[Rh_2(espn)_2(L)_n]^{m+}$, **3_(L)$_n$** [where L = none with $m = 1$; L = $H_2O$, $n = 1$ or 2 with $m = 1$; L = $Cl^-$, $n = 1$ with $m = 0$; and L = $Cl^-$, $n = 2$, with $m = -1$] species by EPR spectroscopy and, where applicable, Cl K-edge XAS, as well as by computational approaches including density functional theory (DFT) and ab initio state-averaged complete active space self-consistent field methods (SA-CASSCF), where necessary. Dynamic electronic correlation effects were included by utilizing multireference difference-dedicated configuration interaction theory with two degrees of freedom (MR-DDCI2). We also elucidate the impact of the nature of the GES of these $Rh_2$(II,III) complexes to the stability and reactivity of their proposed nitrene intermediates by investigating intramolecular C–H amination catalyzed by **2_L** and **3_L** species. Although it is instructive to compare the GES of **2_L** and **3_L** with that of the simplified **1_L** species, the latter species are not included in the reactivity studies because NTC by **1_L** has not been established to utilize the $Rh_2$(II,III) oxidation state.

## 2. RESULTS AND DISCUSSION

**2.1. Analysis of the $Rh_2$(II,III) Compounds.** *2.1.1. Electronic Structure of $Rh_2$(II,III) Complexes.* At first, we elucidated the GES of the $Rh_2$(II,III) complexes using the BP86 density functional method in conjunction with TZVP basis sets[51] for optimization of geometries. Reported DFT energies were derived from single-point B3LYP calculations on the BP86-optimized structures.[52−55] Redox potential calculations were performed using an established methodology.[56] MR-DDCI2:-SA-CASSCF calculations were performed using various active spaces (see the Computational Methods section for more details).

*2.1.1.1. $[Rh_2(OAc)_4(L)_n]^{m+}$, 1_(L)$_n$ Species.* We start our discussion with $Rh_2$(II,III) tetra-acetate complexes $[Rh_2(OAc)_4]^+$, **1**, $[Rh_2(OAc)_4(H_2O)_2]^+$, **1_(H$_2$O)$_2$**, $[Rh_2(OAc)_4Cl]$, **1_Cl**, and $[Rh_2(OAc)_4(Cl)_2]^-$, **1_Cl$_2$**. Herein, we mostly focus on **1_(H$_2$O)$_2$** and **1_Cl$_2$** for which experimental data are available, but we also compare those to **1** to gauge the effect of axial ligand coordination to the $Rh_2$(II,III) core. EPR spectra of $[Rh_2(OAc)_4(L)_n]^{m+}$ have been reported with L = $H_2O$, EtOH, and THF with $n = 2$ and $m = 1$, and Cl with $n = 2$ and $m = -1$. The spectra are axial with $g_\parallel$ = 3.38–4.00 and $g_\perp$ = 0.6–1.5.[48] These unusual $g$ values are described by Kawamura and co-workers as the result of a first-order spin–orbit interaction derived from the nearly degenerate $\pi^*$ orbitals of the $^2E_g$ state, but computational support for these phenomenological assignments is lacking.[46−49]

To validate DFT methods against these experimental data, the GES and EPR parameters for the compounds **1**, **1_(H$_2$O)$_2$**, **1_Cl**, and **1_(Cl)$_2$** were calculated. These DFT calculations converged to the expected $^2E_g$ GES for all four complexes.[57] However, despite predicting the anticipated $^2E_g$ ground state,


DOI: 10.1021/jacs.5b12790
J. Am. Chem. Soc. 2016, 138, 2327–2341

**Table 1. Calculated and Experimentally Measured EPR Parameters of the $[Rh_2(OAc)_4(L)_n]^{m+}$, 1_L, Species (L = None, $H_2O$, and $Cl^-$)**

| species | $g_1$ | $g_2$ | $g_3$ | methods |
|---|---|---|---|---|
| $[Rh_2(OAc)_4]^+$ | 7.36 | 2.61 | 2.04 | RI-B3LYP |
| | 4.00 | 0.05 | 0.05 | MR-DDCI2:SA-CASSCF(13e/8o) |
| $[Rh_2(OAc)_4(H_2O)_2]^+$ | 3.61 | 1.50 | 1.50 | experiment[48] |
| | 3.41 | 2.32 | 2.07 | RI-B3LYP |
| | 3.83 | 0.87 | 0.87 | MR-DDCI2:SA-CASSCF(17e/10o) |
| $Rh_2(OAc)_4Cl$ | 27.4 | 2.43 | 2.13 | RI-B3LYP |
| | 3.99 | 0.18 | 0.18 | MR-DDCI2:SA-CASSCF(19e/11o) |
| $[Rh_2(OAc)_4(Cl)_2]^{-a}$ | 4.00 | 0.60 | 0.60 | experiment[48] |
| | 18.5 | 2.77 | 2.14 | RI-B3LYP |
| | 4.01 | 0.01 | 0.01 | MR-DDCI2:SA-CASSCF(25e/14o) |
| $[Rh_2(esp)_2]^-$ | 2.14 | 2.14 | 1.93 | experiment (this work) |
| | 2.25 | 2.25 | 1.89 | experiment (this work) |
| | 2.24 | 2.11 | 2.06 | RI-B3LYP |

[a]No crystal structure of $[Rh_2(OAc)_4(Cl)_2]^-$ was available, so the geometry was obtained from the structure of $[Rh_2(OAc)_4Cl_2]^{2-}$.[105]

**Table 2. Leading Configurations in the SA-CASSCF Wave Functions of $[Rh_2(OAc)_4(L)_n]^{m+}$, 1_L, Species (L = None, $H_2O$, and $Cl^-$)[a]**

| compound | active space | CSFs[b] | weight (%) |
|---|---|---|---|
| $[Rh_2(OAc)_4]^+$ | (13,8) | $\delta^2\delta^{*2}\pi_1^2\pi_2^2\sigma^2\pi^*_1{}^2\pi^*_2{}^1\sigma^{*0}$ | 43.3 |
| | | $\delta^2\delta^{*2}\pi_1^2\pi_2^2\sigma^2\pi^*_1{}^1\pi^*_2{}^2\sigma^{*0}$ | 43.3 |
| $[Rh_2(OAc)_4(H_2O)_2]^+$ | (17,10) | $\pi^*_{2,+}{}^2\sigma^*_+{}^2\delta^2\delta^{*2}\pi_1^2\pi_2^2\sigma^2\pi^*_1{}^2\pi^*_{2,-}{}^1\sigma^*_-{}^0$ | 43.5 |
| | | $\pi^*_{2,+}{}^2\sigma^*_+{}^2\delta^2\delta^{*2}\pi_1^2\pi_2^2\sigma^2\pi^*_1{}^1\pi^*_{2,-}{}^2\sigma^*_-{}^0$ | 43.5 |
| | | $\pi^*_{2,+}{}^2\sigma^*_+{}^2\delta^2\delta^{*2}\pi_1^u\pi_2^2\sigma^d\pi^*_1{}^2\pi^*_{2,-}{}^2\sigma^*_-{}^u$ | 4.6 |
| | | $\pi^*_{2,+}{}^2\sigma^*_+{}^2\delta^2\delta^{*2}\pi_1^2\pi_2^u\sigma^d\pi^*_1{}^2\pi^*_{2,-}{}^2\sigma^*_-{}^u$ | 4.6 |
| $Rh_2(OAc)_4Cl$ | (19,11) | $\delta^2\delta^{*2}\pi_1^2\pi_2^2\pi_{1,nb}^2\pi_{2,nb}^2\sigma^2\sigma_{nb}^2\pi^*_1{}^2\pi^*_2{}^1\sigma^{*0}$ | 41.9 |
| | | $\delta^2\delta^{*2}\pi_1^2\pi_2^2\pi_{1,nb}^2\pi_{2,nb}^2\sigma^2\sigma_{nb}^2\pi^*_1{}^1\pi^*_2{}^2\sigma^{*0}$ | 41.9 |
| | | $\delta^2\delta^{*2}\pi_1^2\pi_2^2\pi_{1,nb}^2\pi_{2,nb}^2\sigma^2\sigma_{nb}^0\pi^*_1{}^2\pi^*_2{}^1\sigma^{*2}$ | 4.2 |
| | | $\delta^2\delta^{*2}\pi_1^2\pi_2^2\pi_{1,nb}^2\pi_{2,nb}^2\sigma^2\sigma_{nb}^0\pi^*_1{}^1\pi^*_2{}^2\sigma^{*2}$ | 4.2 |
| $[Rh_2(OAc)_4Cl_2]^{-c}$ | (25,14) | $\pi_{1,+}{}^2\pi_{2,+}{}^2\pi^*_{1,+}{}^2\pi^*_{2,+}{}^2\sigma_+{}^2\delta^2\delta^{*2}\sigma^*_+{}^2\pi_{1,-}{}^2\pi_{2,-}{}^2\sigma_-{}^2\pi^*_{1,-}{}^2\pi^*_{2,-}{}^1\sigma^*_-{}^0$ | 43.2 |
| | | $\pi_{1,+}{}^2\pi_{2,+}{}^2\pi^*_{1,+}{}^2\pi^*_{2,+}{}^2\sigma_+{}^2\delta^2\delta^{*2}\sigma^*_+{}^2\pi_{1,-}{}^2\pi_{2,-}{}^2\sigma_-{}^2\pi^*_{1,-}{}^1\pi^*_{2,-}{}^2\sigma^*_-{}^0$ | 42.8 |
| | | $\pi_{1,+}{}^2\pi_{2,+}{}^2\pi^*_{1,+}{}^2\pi^*_{2,+}{}^2\sigma_+{}^2\delta^2\delta^{*2}\sigma^*_+{}^2\pi_{1,-}{}^u\pi_{2,-}{}^2\sigma_-{}^d\pi^*_{1,-}{}^2\pi^*_{2,-}{}^1\sigma^*_-{}^u$ | 5.0 |
| | | $\pi_{1,+}{}^2\pi_{2,+}{}^2\pi^*_{1,+}{}^2\pi^*_{2,+}{}^2\sigma_+{}^2\delta^2\delta^{*2}\sigma^*_+{}^2\pi_{1,-}{}^0\pi_{2,-}{}^u\sigma_-{}^d\pi^*_{1,-}{}^2\pi^*_{2,-}{}^1\sigma^*_-{}^u$ | 5.0 |

[a]Configurations with weight >3% are reported. [b]CSFs = configuration state functions. All orbital symbols have their normal meaning; nb = nonbonding, + and − refer to in-phase and out-of-phase contributions of the equatorial ligands. [c]Geometry for the single-point calculation was obtained without further optimization from the crystal structure of $[(NH_2)_3C]_2[Rh_2(OAc)_4Cl_2]$.[105]

the DFT-calculated EPR $g$ values are incompatible with the available experimental data: DFT predicts a markedly rhombic $g$ tensor with abnormal values, giving $g_1$, $g_2$, and $g_3$ of 7.36, 2.61, and 2.04 for **1**, 3.41, 2.32, and 2.07 for **1_(H$_2$O)$_2$**, 27.4, 2.43, and 2.13 for **1_Cl**, and 18.5, 2.77, and 2.14 for **1_Cl$_2$**, respectively, whereas the experimental spectra are axial with $g_{\parallel} \sim 4.00$ and $g_{\perp} \ll 2.00$ (see Table 1).

The aforementioned discrepancy between the experimental and DFT findings can be explained by the multideterminant nature of the $^2E_g$ electronic state, where the energetic degeneracy of the $\pi^*$ orbitals presents an inherent problem for all single-determinant-based methods, including DFT.[58] Indeed, a "proper" wave function of the $^2E_g$ electronic state should include, at least, the following two simplified determinants

$$\Psi(^2E_g) = \frac{1}{\sqrt{2}}[|(\pi_1^*)^2(\pi_2^*)^1| + |(\pi_1^*)^1(\pi_2^*)^2|] \quad (1)$$

because the unpaired electron has an equal probability of being housed in either the $\pi_1^*$ or the $\pi_2^*$ orbital. In order to properly describe such a multideterminant system allowing for an accurate prediction of $g$ tensors of the complexes, the CASSCF approach is utilized.

The leading determinants of the SA-CASSCF wave functions with their weights are given in Table 2. For all **1_L** compounds, there are two leading determinants that contribute equally, or nearly equally, to their total wave functions. In all cases, these two leading determinants are those that differ in their $\pi_1^*$ and $\pi_2^*$ occupation, as anticipated from the above discussion. Thus, the CASSCF results are fully consistent with $^2E_g$-derived ground states for these compounds.


DOI: 10.1021/jacs.5b12790
J. Am. Chem. Soc. 2016, 138, 2327−2341

The MR-DDCI2 method was used on the converged SA-CASSCF wave function to predict the $g$ values of $[Rh_2(OAc)_4]^+$: an axial signal with $g_{\|} = 4.00$ and $g_{\perp} = 0.05$ is predicted. As seen in Table 1, where we provide all calculated and experimental $g$ values for $[Rh_2(OAc)_4]^+$, $[Rh_2(OAc)_4(H_2O)_2]^+$, $Rh_2(OAc)_4Cl$, and $[Rh_2(OAc)_4Cl_2]^-$, the MR-DDCI2:SA-CASSCF-calculated EPR $g$ values are in close agreement with the experimental values. These findings additionally support that all of these species have a $^2E_g$ ground state containing a $(\pi^*)^3$ valence electron configuration.

Thus, due to existence of the orbital degeneracy in **1_L**$^+$, the DFT approach is not the best method to calculate the lowest-energy electronic states and related properties of these compounds.

*2.1.1.2. $[Rh_2(esp)_2L]^+$.* To date, only one set of crystallographic data is available for a metastable Rh$_2$(II,III) complex bearing esp ligands, $[Rh_2(esp)_2Cl_2]^-$.[39] In this paper, we report optimized geometries of the species $[Rh_2(esp)_2]^+$, **2**, $[Rh_2(esp)_2(H_2O)]^+$, **2_H$_2$O**, and $Rh_2(esp)_2Cl$, **2_Cl**. In Table 3, we compare the optimized parameters of these species with the available crystallographic values. As seen from this table, the DFT approach describes the Rh−Rh and Rh−O$_{av}$ distances well.

**Table 3. Calculated and Experimentally Available Important Geometry Parameters (Distances in Å and Angles in deg) of the $[Rh_2(esp)_2L]^+$, 2_L, Species (L = None, $H_2O$, and $Cl^-$)**

| species | Rh−Rh | Rh−L | Rh−O$_{av}$ | Rh−Rh−L |
|---|---|---|---|---|
| Calculated: This work | | | | |
| $[Rh_2(esp)_2]^+$ | 2.362 | | 2.041 | |
| $[Rh_2(esp)_2(H_2O)]^+$ | 2.378 | 2.253 | 2.043 | 178.9 |
| $Rh_2(esp)_2Cl$ | 2.394 | 2.361 | 2.065 | 180.0 |
| Experiment[39] | | | | |
| $[Rh_2(esp)_2(Cl)_2]^-$ | 2.360(1) | 2.475(1) | 2.023(1) | 174.4(1) |

DFT calculations on **2** surprisingly predict a $^2B_{1u}$-derived GES with a $(\delta^*)^1$ electron configuration. Analysis shows that in this compound, like in the case of the $[Rh_2(OAc)_4]^+$ complexes, the $\delta^*$ orbital has significant antibonding contributions from the O−C−O $\pi^*$ carboxylate (bridging) orbitals. However, unlike the case of $[Rh_2(OAc)_4]^+$ complexes, the $\delta^*$ orbital of **2** also has a contribution from the *m*-phenylene moieties of the esp ligands, an apparent through-space interaction at 4.3 Å. This interaction slightly destabilizes the $\delta^*$ orbital, and, consequently, makes the $^2B_{1u}$-type $(\delta^*)^1$ electronic state more favorable for $[Rh_2(esp)_2]^+$ compared to the $[Rh_2(OAc)_4]^+$ complexes.

To experimentally substantiate the computationally predicted $^2B_{1u}$-derived ground state with a $(\delta^*)^1$ orbital configuration of **2**, we turned our attention to spectroscopic studies. As shown previously, $Rh_2(esp)_2$ is not stable in the Rh$_2$(II,III) redox state, but in $CH_2Cl_2$ solution, it can be oxidized coulometrically to the corresponding Rh$_2$(II,III) species **2**.[39] The coulometric oxidation was monitored by UV−vis spectroscopy, which showed near-isosbestic behavior indicative of oxidation to an isostructural product with the possibility of a partial transformation of the oxidized product via a chemical reaction. A sample of electrochemically generated **2** was frozen upon generation and analyzed by EPR spectroscopy. The EPR spectrum given in Figure 1 is surprising in two ways. First, the spectrum cannot be simulated by a single $S = 1/2$ species and therefore indicates that **2** actually contains *two* Rh$_2$(II,III) species that are similar in structure, as evidenced by the similarity of their axially symmetric EPR signals. Second, the best-simulated EPR $g$ values, $g_{\perp} = 2.124$ and $g_{\|} = 1.928$ for the first species and $g_{\perp} = 2.255$ and $g_{\|} = 1.893$ for the second species, are indicative of a relatively simple $S = 1/2$ species with a single Kramers' doublet, excluding the possibility of having a ground state with the $(\pi^*)^3$ orbital configuration for **2**. The observed $g$ values instead fit well in the range of those observed for compounds with a ground state containing a $(\delta^*)^1$ orbital.[50] As for the reason that two EPR-active species are produced during coulometric oxidation of $[Rh_2(esp)_2]$, this is likely due to partial coordination of a solvent or electrolyte species in the axial site of the Rh$_2$ molecule to generate Rh$_2$ species such as $Rh_2(esp)_2Cl$, which has been observed in a high-resolution mass spectrum,[35] and is consistent with the imperfect isosbestic behavior of the oxidation. Notably, the EPR parameters predicted by DFT for **2**, $g_1 = 2.24$, $g_2 = 2.11$, $g_3 = 2.06$, differ in symmetry but are close to the experimental values.

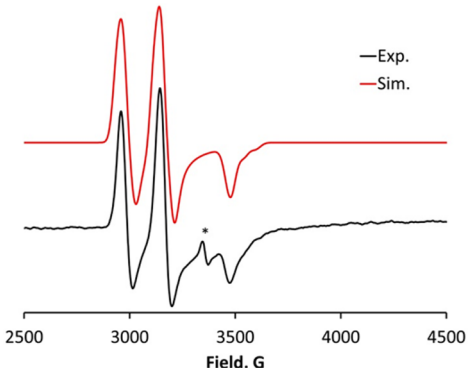


**Figure 1.** X-band EPR spectrum measured at 10 K of an electrochemically oxidized solution of $Rh_2(esp)_2$. The spectrum is modeled with two axially symmetric subspecies present in a 1:1 ratio. Species 1: $g_{\perp} = 2.124$, $g_{\|} = 1.928$, $A_{\perp} = 95$ MHz. Species 2: $g_{\perp} = 2.255$, $g_{\|} = 1.893$, $A_{\perp} = 93$ MHz, $A_{\|} = 150$ MHz. Instrument parameters: mw frequency = 9.3814 GHz, power = 0.6325 dB, attenuation = 25 dB, modulation frequency = 100 kHz, modulation amplitude = 4 G, receiver gain = 70 dB, time constant = 163.84 ms, conversion time = 10 ms.

Comparison of the DFT-calculated electronic state and aforementioned EPR data clearly shows that the utilized DFT approach provides an adequate description of the ground state wave function of **2** and its derivatives. Thus, DFT can be used to further explore the chemistry of these species.

*2.1.1.3. $[Rh_2(espn)_2L]^+$, 3_L.* Recently, Berry and co-workers have reported a new amidate-ligated catalyst, $Rh_2(espn)_2Cl$, **3_Cl**, which can form as any one of four possible isomers: the (*cis*-2,2)-, (4,0)-, (*trans*-2,2)-, and (3,1)-isomers. However, the synthesis of **3_Cl** results in two structural isomers (*cis*-2,2)-(**3_Cl**) and (4,0)-(**3_Cl**), with the *cis*-2,2 isomer favored in a 4:1 ratio.[40] At low concentrations, **3_Cl** dissociates $Cl^-$ in $CH_2Cl_2$ to form $[Rh_2(espn)_2]^+$, **3**, and it was possible to assign electrochemical features to both the Cl-bound and unbound species.[40]

We report here experimental EPR and XAS measurements aimed at elucidating the nature of the ground state of **3**. EPR data on the $[Rh_2(espn)_2L]^+$ complexes in solution are consistent with an $S = 1/2$ ground state for these species. Indeed, the spectra of these compounds can be straightforwardly simulated by near-axial $S = 1/2$ signals showing $^{103}$Rh hyperfine splitting of the $g_{\|}$ signal. The best simulations of these


DOI: 10.1021/jacs.5b12790
J. Am. Chem. Soc. 2016, 138, 2327−2341

spectra yield the following parameters: $g_\perp = 2.11$, $g_\parallel = 1.927$, $A_\parallel = 90$ MHz for (*cis*-2,2)-(**3_Cl**) and $g_\perp = 2.105$, $g_\parallel = 1.905$, $A_\parallel = 135$ MHz for (4,0)-(**3_Cl**) (see Figure 2). Our results compare

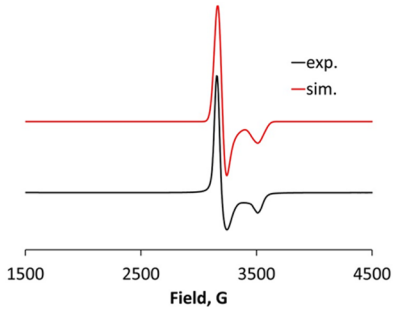


**Figure 2.** X-band EPR spectrum measured at 10 K of 4,0-$Rh_2$(espn)$_2$Cl. The spectrum is modeled with $g_\perp = 2.105$, $g_\parallel = 1.905$, and $A_\parallel = 135$ MHz. Instrument parameters: mw frequency = 9.3792 GHz, power = 0.6385 mW, attenuation = 25.0 dB, modulation frequency = 100 kHz, modulation amplitude = 4 G, receiver gain = 30 dB, time constant = 327.68 ms, conversion time = 10.0 ms.

favorably with those reported by Kadish, Bear, and co-workers on $Rh_2$(II,III) acetamidate analogues, which have $g_\perp = 2.11-2.13$, $g_\parallel = 1.89-1.92$, and $A_\parallel = 79-90$ MHz.[50] These data support the assignment of the GES with a $(\delta^*)^1$ configuration for **3**.

Another spectroscopic method that has not yet been used with metal−metal bonded compounds but, in principle, can distinguish between the $(\pi^*)^3$ and $(\delta^*)^1$ states in [$Rh_2$(II,III)]−Cl complexes is Cl K-edge X-ray absorption spectroscopy (XAS). Cl K-pre-edge transitions may be formally assigned as Cl 1s → "$\varphi$", where $\varphi$ represents a molecular orbital of the form $[\alpha(\text{Rh 4d}) + \sqrt{1-\alpha^2}\ (\text{Cl 3p})]$. Here, the presence of Cl 3p character in partially unoccupied valence orbitals is required for nonzero Cl K-pre-edge intensity. From symmetry considerations, Cl character can be mixed into $\sigma$- or $\pi$-type orbitals in a linear Rh−Rh−Cl structure but cannot be mixed into $\delta$-symmetry orbitals. Thus, a $(\pi^*)^3$ compound should display a pre-edge feature below the main $\sigma^*$ transition corresponding to the partially filled $Rh_2$ $\pi^*$ level, and a $(\delta^*)^1$ compound should not. Thus, in the case of the anticipated $(\delta^*)^1$ ground state of **3_Cl**, we expect to observe a Cl 1s → $\sigma^*$ pre-edge transition, whereas with a $(\pi^*)^3$ ground state, there would be an additional, resolvable lower-energy transition: Cl 1s → $\pi^*$. The Cl pre-edge region for **3_Cl** is shown along with its corresponding second-derivative plot and least-squares fit in Figure 3. The pre-edge region comprises a single peak at 2822.1 eV. The presence of a single peak is consistent with a GES having a Rh−Rh $\delta^*$ SOMO.

To support these experimental results, we have computationally investigated the (*cis*-2,2)- and (4,0)-isomers of [$Rh_2$(espn)$_2$]$^+$, **3**, [$Rh_2$(espn)$_2$($H_2O$)]$^+$, **3_$H_2O$**, and $Rh_2$(espn)$_2$Cl, **3_Cl** species. Their calculated and experimental geometries at the ground doublet electronic states (with the unpaired electron in the Rh−Rh $\delta^*$ orbital) are given in Table 4. One should mention that the (4,0)-(**3_L**) species could have two isomers, which differ by coordination of the L ligand to the $Rh_2$ center surrounded by either four N centers or four O centers. Below, we call these isomers $(4,0)_N$ and $(4,0)_O$, respectively. In general, the $(4,0)_N$-isomer is found to be energetically a few kJ/mol more favorable than the $(4,0)_O$-isomer for both doublet and quartet state species. The energy

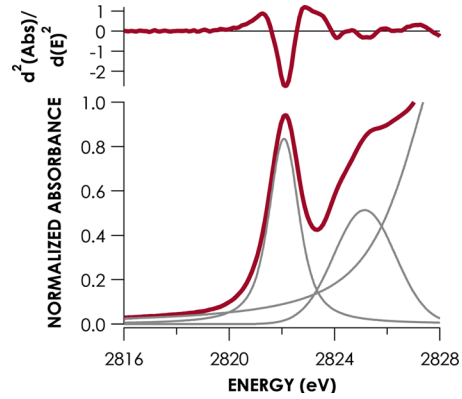


**Figure 3.** Pre-edge region and second derivative plot of (*cis*-2,2)-$Rh_2$(espn)$_2$Cl Cl K-edge XAS. Pseudo-Voigt peaks are shown in gray.

difference between these isomers is slightly larger for L = Cl than $H_2O$. For simplicity, below we discuss only the energetically more stable $(4,0)_N$-isomers of **3_$H_2O$** and **3_Cl** species, but we include all energy and geometry results for the less stable $(4,0)_O$-isomers of **3_$H_2O$** and **3_Cl** in the Supporting Information.

As seen from Table 4, in general, the calculated geometries of the doublet $S = 1/2$ GESs of **3**, **3_$H_2O$**, and **3_Cl** with the unpaired electron in the Rh−Rh $\delta^*$ orbital match closely their experimental values. One major disagreement between the calculated and experimental structures occurs for (*cis*-2,2)-(**3_Cl**): the experimental structure of this species is polymeric, with $Cl^-$ ions bridging an infinite chain of $Rh_2$ species. In contrast, its calculated structure is molecular with a monodentate $Cl^-$ ligand. As a result, the Rh−Cl bond distance is severely underestimated in the calculation, which, in turn, leads to an overestimation of the Rh−Rh bond distance. Since the Cl-bridged structure is a feature only of the solid-state packing of this compound and is likely absent in homogeneous solution, the calculated structure is presumably a more accurate model for the compound in solution during catalysis.

After elucidating the electronic and geometric structures of the aforementioned $Rh_2$(II,III) species, we are well-positioned to discuss their redox potentials, which are vital for understanding the stability and reactivity of these species. Based on the above-presented comparison of DFT and experimental data, one may confidently use DFT methods to calculate redox potentials and provide insight into the proclivity for axial ligand binding of the $Rh_2$(II,III) species **2_L** and **3_L**. We excluded **1_L** species from reactivity studies due to the facts that (a) NTC by **1_L** has not been established to utilize the $Rh_2$(II,III) oxidation state and (b) the GES of **1** is multiconfigurational and, therefore, may not be accurately described by the DFT approach.

*2.1.2. Energy Landscape: Redox Potentials and Axial Ligand Effects.* For [$Rh_2$(esp)$_2$]$^+$, **2**, experiments showed that the $\mathbf{2}^{0/+}$ redox potential is at 0.80 V vs Fc/Fc$^+$.[39,59] DFT predicts a value of 0.78 V, which is in excellent agreement with the experimental value (see Scheme 2). The calculated $[\mathbf{2\_Cl}]^{0/-}$ redox potential is −0.72 V vs Fc/Fc$^+$. Since previous experiments showed that **2** strongly binds $Cl^-$ ions,[35] we also calculated the impact of a second $Cl^-$ ligand binding to [$Rh_2$(esp)$_2$]$^+$, **2**. It was found that the binding of two $Cl^-$ ligands to **2** greatly lowers the $Rh_2$(II,II)/$Rh_2$(II,III) (in short, $Rh_2^{4+/5+}$) redox potential by 2.27 V. These findings show that increasing the concentration of chloride (or any other anionic


DOI: 10.1021/jacs.5b12790
J. Am. Chem. Soc. 2016, 138, 2327−2341

Table 4. Calculated and Experimentally Available Important Geometry Parameters (Distances in Å) of the (*cis*-2,2) and (4,0) Isomers of $[Rh_2(espn)_2L]^+$, 3_L, Species (L = None, $H_2O$, and $Cl^-$), at Their Lower-Lying Doublet ($S$ = 1/2) and Quartet ($S$ = 3/2) Electronic States

| species | Rh−Rh | Rh−$L_{ax}$ | Rh−$N_{eq}$ | Rh−$O_{eq}$ | $S$ |
|---|---|---|---|---|---|
| | | Calculated: This work | | | |
| (*cis*-2,2)-$[Rh_2(espn)_2]^+$ | 2.40 | | 2.02 | 2.05 | 1/2 |
| | 2.47 | | 2.03 | 2.06 | 3/2 |
| (*cis*-2,2)-$[Rh_2(espn)_2(H_2O)]^+$ | 2.41 | 2.28 | 2.02 | 2.06 | 1/2 |
| | 2.48 | 2.48 | 2.03 | 2.08 | 3/2 |
| (*cis*-2,2)-$[Rh_2(espn)_2Cl]$ | 2.46 | 2.42 | 2.01 | 2.08 | 1/2 |
| | 2.54 | 2.62 | 2.02 | 2.08 | 3/2 |
| | | Experiment[40] | | | |
| (*cis*-2,2)-$[Rh_2(espn)_2Cl]_n$ | 2.4155(9) | 2.617(2) | 1.970(6) | 2.033(5) | 1/2 |
| | | Calculated: This work | | | |
| (4,0)-$[Rh_2(espn)_2]^+$ | 2.40 | | 2.05 | 2.03 | 1/2 |
| | 2.47 | | 2.05 | 2.03 | 3/2 |
| (4,0)-$[Rh_2(espn)_2(H_2O)]^+$ | 2.41 | 2.34 | 2.05 | 2.03 | 1/2 |
| | 2.50 | 2.43 | 2.05 | 2.05 | 3/2 |
| (4,0)-$[Rh_2(espn)_2Cl]$ | 2.44 | 2.44 | 2.04 | 2.04 | 1/2 |
| | 2.51 | 2.55 | 2.07 | 2.05 | 3/2 |
| | | Experiment[40] | | | |
| (4,0)-$[Rh_2(espn)_2Cl]$ | 2.4136(4) | 2.6165(9) | 2.003(3) | 1.998(2) | 1/2 |

Scheme 2. Energy Landscape of Compounds 2, 2_Cl, and 2_$Cl_2$[a]

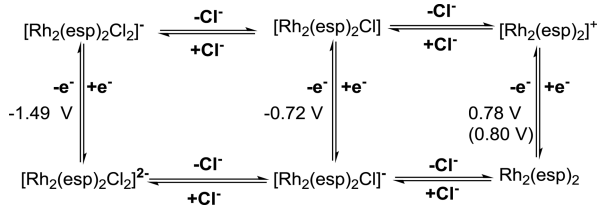


[a]DFT-calculated and experimental redox potentials are given without and with parentheses, respectively.

potential axial ligand for that matter) in reaction mixture could strongly favor catalysis in the $Rh_2$(II,III) regime, though if the concentrations are too high, catalysis could be hindered by blocking of both axial sites.

As mentioned above, experiments showed that complex **3_Cl** could have several isomers among which the (*cis*-2,2)- and (4,0)-isomers are experimentally observed, with the *cis*-2,2-isomer favored in a 4:1 ratio.[40] Consistent with this finding, DFT calculations predict the (*cis*-2,2)_(**3_Cl**)-isomer to be lower in energy than the (4,0)-isomer by 12.1 kJ/mol (see Scheme 3). Dissociation of the axial chloride ligand leads to the active cationic catalyst, $[Rh_2(espn)_2]^+$, the (*cis*-2,2)-**3** isomer of which is higher in energy by 15.5 kJ/mol than its (4,0)-**3**-isomer. The four nitrogen atoms bound to the high-oxidation state $Rh^{III}$ center in the (4,0)-isomer, therefore, appear to provide greater stabilization to the Rh atom than two nitrogen and two oxygen atoms than in the (2,2)-isomer.

Cyclic voltammetry experiments were performed for (*cis*-2,2)-**3**, which showed two reversible waves corresponding to $[Rh_2(espn)_2]^{0/+}$ at −0.33 V and $[Rh_2(espn)_2]^{+/2+}$ at 1.01 V. A third quasi-reversible peak was observed at 0.60 V, which was assigned to the chloride-bound $[Rh_2(espn)_2Cl]^{0/+}$ redox

Scheme 3. Energy Landscape of Compounds (*cis*-2,2)-3, (*cis*-2,2)-(3_Cl), (4,0)-3, and (4,0)-(3_Cl)[a]

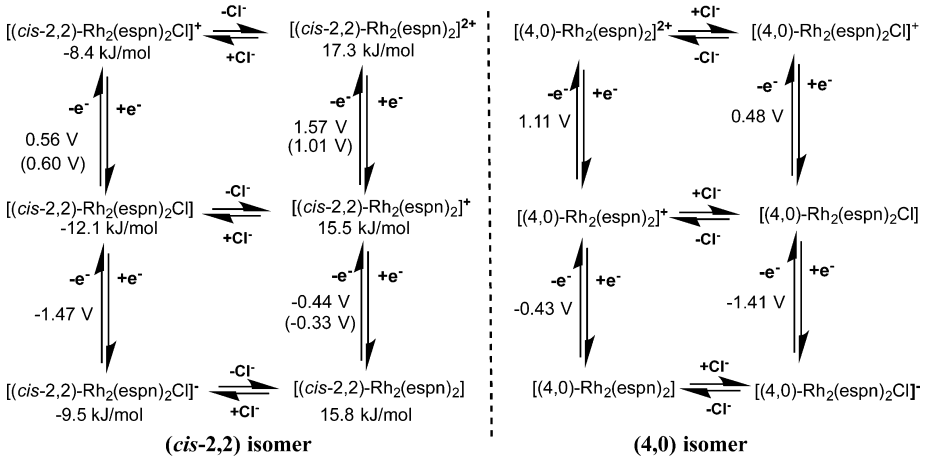


[a]DFT-calculated and experimental redox potentials (listed relative to the $Fc/Fc^+$ couple) are given without and with parentheses, respectively. Presented relative energies (in kJ/mol) are listed relative to the corresponding (4,0)-isomers.



DOI: 10.1021/jacs.5b12790
J. Am. Chem. Soc. 2016, 138, 2327−2341

Table 5. Calculated Important Geometry Parameters (Distances in Å and Angles in deg) of the $\{Rh_2(esp)_2[NSO_3(CH_2)_3Ph](L)\}^+$, 2N_L, Species (L = None, $H_2O$, and $Cl^-$), at Their Doublet ($S$ = 1/2) and Quartet ($S$ = 3/2) Electronic States

| species | $S$ | Rh−Rh | Rh−N | Rh−L | Rh−Rh−L | Rh−Rh−N | Rh−N−S |
|---|---|---|---|---|---|---|---|
| **2N** | 1/2 | 2.40 | 1.92 | | | 176 | 122 |
| | 3/2 | 2.42 | 1.95 | | | 172 | 125 |
| **2N_$H_2O$** | 1/2 | 2.39 | 1.93 | 2.31 | 167 | 170 | 129 |
| | 3/2 | 2.42 | 2.00 | 2.35 | 174 | 170 | 126 |
| **2N_Cl** | 1/2 | 2.44 | 1.93 | 2.34 | 165 | 161 | 126 |
| | 3/2 | 2.46 | 2.03 | 2.40 | 172 | 169 | 124 |

Table 6. Calculated Important Geometry Parameters (Distances in Å and Angles in deg) of the $\{Rh_2(espn)_2[NSO_3(CH_2)_3Ph](L)\}^+$, 3_L, Species (L = None, $H_2O$, and $Cl^-$), at Their Doublet ($S$ = 1/2) and Quartet ($S$ = 3/2) Electronic States

| species | $S$ | Rh−Rh | Rh−$N_{ax}$ | Rh−$L_{ax}$ | Rh−$N_{eq}$ | Rh−$O_{eq}$ | Rh−Rh−L | Rh−Rh−N | Rh−N−S |
|---|---|---|---|---|---|---|---|---|---|
| (*cis*-2,2)-**3N** | 1/2 | 2.46 | 1.94 | | 2.02 | 2.08 | | 174 | 119 |
| | 3/2 | 2.45 | 1.94 | | 2.02 | 2.09 | | 173 | 119 |
| (*cis*-2,2)-**3N_$H_2O$** | 1/2 | 2.44 | 1.99 | 2.39 | 2.03 | 2.07 | 174 | 171 | 129 |
| | 3/2 | 2.44 | 1.98 | 2.39 | 2.03 | 2.07 | 175 | 171 | 127 |
| (*cis*-2,2)-**3N_Cl** | 1/2 | 2.48 | 2.04 | 2.45 | 2.02 | 2.08 | 167 | 172 | 123 |
| | 3/2 | 2.48 | 2.03 | 2.46 | 2.02 | 2.09 | 166 | 172 | 123 |
| (4,0)-**3N** | 1/2 | 2.48 | 1.92 | | 2.04 | 2.07 | | 176 | 117 |
| | 3/2 | 2.43 | 1.96 | | 2.05 | 2.02 | | 176 | 127 |
| (4,0)-**3N_$H_2O$** | 1/2 | 2.44 | 2.00 | 2.34 | 2.06 | 2.03 | 174 | 172 | 128 |
| | 3/2 | 2.44 | 2.00 | 2.34 | 2.06 | 2.03 | 175 | 171 | 126 |
| (4,0)-**3N_Cl** | 1/2 | 2.48 | 2.04 | 2.45 | 2.02 | 2.09 | 166 | 172 | 123 |
| | 3/2 | 2.47 | 2.03 | 2.47 | 2.03 | 2.06 | 174 | 170 | 126 |

couple.[40] For (*cis*-2,2)-**3**, DFT calculations predicted the $[Rh_2(espn)_2]^{0/+}$ couple at −0.44 V and the $[Rh_2(espn)_2]^{+/2+}$ couple at 1.57 V. The $[Rh_2(espn)_2Cl]^{0/+}$ couple is predicted at 0.56 V. Here, the agreement between calculated and experimentally measured redox potentials is superb, providing excellent support for the assignments of these waves as well as validation for the DFT methods used (see Computational Methods for more details). The one exception is the redox couple involving the dicationic species $[(cis\text{-}2,2)\text{-}Rh_2(espn)_2]^{2+}$, where the discrepancy is likely the result of stronger solvation effects on the energy of the dication. For the (4,0)-isomer of **3**, the $[Rh_2(espn)_2]^{0/+}$ couple was predicted at −0.43 V and the $[Rh_2(espn)_2]^{+/2+}$ couple at 1.11 V. The $[Rh_2(espn)_2Cl]^{0/+}$ couple was predicted at 0.48 V. All of the calculated and measured redox potentials are summarized in Scheme 3.

This analysis of $Rh_2$ electronic states and redox potentials now positions us to investigate catalytically relevant intermediates of the mixed-valent $Rh_2$(II,III) complexes **2_L** and **3_L** and study intimate mechanistic details of C−H amination catalyzed by these systems, where L = none, $H_2O$, and Cl.

**2.2. $Rh_2$(II,III) Nitrene Complexes and Mechanism of Intramolecular C−H Amination.** *2.2.1. Electronic Structure of the $Rh_2$(II,III)-Nitrene Intermediates.* As mentioned above (see Scheme 1), one of the most important intermediates of both intra- and intermolecular C−H amination by the mixed-valent $Rh_2$(II,III) species under oxidative NTC conditions is the transient $Rh_2$(II,III)-nitrene complex. Since isolation and characterization of these transient complexes has, to date, not been possible, DFT and CASSCF computations, validated above, appear to be the most valuable tool to study the electronic and geometric structures, as well as reactivity of these species.

DFT calculations were used to optimize structures of the **2N_L** and **3N_L** nitrene complexes of the species **2_L** and **3_L**, respectively, as described in more detail in the Computational Methods section. The results are given in Tables 5 and 6. In all structures, the Rh−Rh distances of 2.39−2.48 Å are not much changed from those of **2_L** and **3_L**. Importantly, the addition of an **L** ligand has little effect on the Rh−Rh distances but elongates the Rh−$N_{ax}$ bond distance, more notably in the doublet state for **2N_L**, but the effect is seen in both spin states of **3N_L** compounds. Interestingly, in doublet **2N**, the $C^1$−$H^1$ bond of the nitrene fragment interacts with the N center and, already, is partly activated with $C^1$−$H^1$, N−$H^1$, and Rh−N distances of 1.15, 1.65, and 1.92 Å, respectively (see also Figure 8).

In all **2N_L** and **3N_L** complexes, the doublet and quartet states are predicted by DFT to be quite close in energy. For the **2N_L** series, the doublet states are predicted to be lowest in energy by 9.6 and 13.8 kJ/mol with L = none and $Cl^-$, respectively. The aquo complex is predicted to have the quartet state lower in energy by (a practically negligible) 4.6 kJ/mol. For the **3N_L** compounds, the quartet states are all lower in energy, presumably due to the higher destabilization of the $\delta^*$ orbital by the more electron-donating equatorial N donors. The energy differences to the doublet states range from 9 to 15 kJ/mol for the *cis*-(2,2)-isomers and from 8 to 11 kJ/mol for the (4,0)-isomers.

In general, the sulfamate-derived nitrene can utilize its $\sigma$ and two $\pi$ orbitals to form bonds with the $\sigma$- and $\pi$-symmetry orbitals of the $Rh_2$(II,III) core, similar to those previously described for $Rh_2$-carbene and $Ru_2$-nitride compounds.[60−68] The important frontier orbitals of the nitrene complexes are the $Rh_2$-centered $\delta^*$ orbital, two three-center Rh−Rh−N $\pi^*$ orbitals, and the three-center Rh−Rh−N $\sigma^*$ orbital (see


DOI: 10.1021/jacs.5b12790
J. Am. Chem. Soc. 2016, 138, 2327−2341

Chart 2). The $\delta^*$ and $\pi^*$ orbitals are expected to be close in energy, as is well-known in other $Rh_2$ and $Ru_2$ systems with a similar electron count.[5,63−67,69] However, the $\pi^*$ orbitals are expected to differ in energy since one of these two orbitals, denoted $\pi^{*\prime}$, is also involved in the N−S bond of the bent nitrene unit. Thus, the similar energies of the doublet or quartet states for the nitrene complexes are derived from configurations with differing population of the $\delta^*$ and $\pi^*$ levels. The configuration of the quartet state is $(\delta^*)^1(\pi^{*\prime})^1(\pi^{*\prime\prime})^1$, but there are several possible doublet configurations to consider. Importantly, the major acceptor orbitals for electrophilic reactivity are the Rh−Rh−N $\pi^*$ orbitals, which are heavily polarized toward the N atoms.

**Chart 2. Molecular Orbital Ordering of [Rh−Rh]−$NSO_3R$ Compounds**[a]

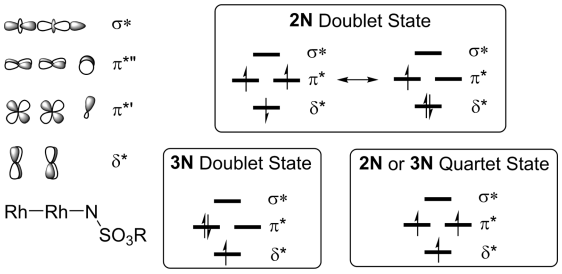


[a]Highlighted electron configurations are of the doublet and quartet states. Only the major electron configuration is shown in each case. Two $\pi^*$ orbitals are shown as degenerate only for simplicity.

Due to the several possible electron configurations for the doublet state, we may expect the doublet states of **2N** and **3N** to be multiconfigurational, with three valence electrons in the near-degenerate $\delta^*$, $\pi^{*\prime}$, and $\pi^{*\prime\prime}$ orbitals. To gauge the importance of this effect, and to extract a useful description of the bonding in these compounds, both DFT and CASSCF calculations on **2N** and **3N** complexes were performed with the simplifying truncation of $CH_3$ for the organic substituent on the nitrene group (labeled **2N′** and **3N′**). Two distinct DFT models for doublet-state **2N′** were considered containing either a singlet or triplet nitrene coordinated to the $Rh_2$ unit. As shown in Table S1, these two configurations are nearly isoenergetic but have drastically different spin distributions. For reference, the DFT frontier orbitals of the singlet nitrene configuration are shown in Figure S1. A similar situation arises when the doublet state of **3N′** is examined by DFT methods (Table S1). Two drastically differing doublet states are found to be different by only ∼8 kJ/mol. Due to the ambiguity in the DFT-calculated electronic structure, further analysis of the bonding in these intermediates was made at the CASSCF level.

The CASSCF electronic configurations of **2N′** and **3N′** and their corresponding weights are given in Tables 7 and 8. The natural orbitals of the multiconfigurational wave function are shown in Figures 4 and 5. Both quartet states are quite similar, with the anticipated $(\delta^*)^1(\pi^{*\prime})^1(\pi^{*\prime\prime})^1$ configurations and spin delocalized throughout the Rh−Rh−N unit. The doublet states of **2N′** and **3N′** are electronically distinct. As seen in Figure 4, there is significant mixing of the orbitals of $\delta^*$ and $\pi^{*\prime\prime}$ symmetry in **2N′** leading to some fluidity in its electronic

**Table 8. Unpaired Spin Populations within the Rh−Rh−N Unit in 2N′ and 3N′, Derived from the CASSCF Wave Functions**

| | | Mulliken spin population[a] | | |
|---|---|---|---|---|
| complex | $S$ | $N$ | $Rh_m$[b] | $Rh_d$[b] |
| **2N′** | 1/2 | 1.05 | 0.12 | −0.23 |
| **2N′** | 3/2 | 1.68 | 0.08 | 1.07 |
| **3N′** | 1/2 | −0.07 | 0.02 | 0.93 |
| **3N′** | 3/2 | 1.09 | 0.55 | 1.12 |

[a]Residual spin populations are located primarily on the $SO_3CH_3$ group. [b]$Rh_m$ = middle rhodium; $Rh_d$ = distal rhodium.

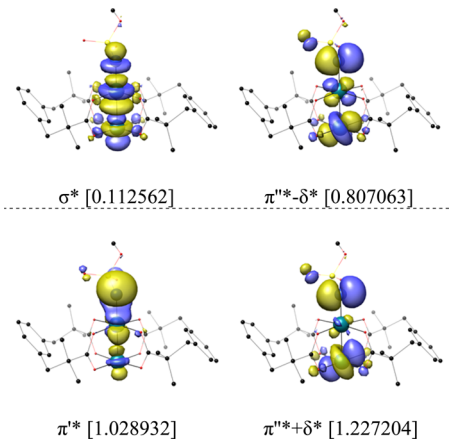


**Figure 4.** Natural frontier orbitals of doublet **2N′** from CASSCF. Occupation numbers are shown in brackets.

**Table 7. Leading Configurations from CASSCF Calculations on 2N′ and 3N′ in Doublet and Quartet States**

| complex | $S$ | active space | CSFs[a] | weight (%) |
|---|---|---|---|---|
| **2N′** | 1/2 | (19,12) | $(\pi''_{nb})^2(\sigma_{nb})^2(\delta^*)^2(\pi'^*)^1(\pi''^*)^0(\sigma^*)^0$ | 46.5 |
| | | | $(\pi''_{nb})^2(\sigma_{nb})^2(\delta^*)^0(\pi'^*)^1(\pi''^*)^2(\sigma^*)^0$ | 26.3 |
| | | | $(\pi''_{nb})^2(\sigma_{nb})^2(\delta^*)^1(\pi'^*)^1(\pi''^*)^1(\sigma^*)^0$ | 16.7 |
| **2N′** | 3/2 | (19,12) | $(\pi''_{nb})^2(\sigma_{nb})^2(\delta^*)^1(\pi'^*)^1(\pi''^*)^1(\sigma^*)^0$ | 90.5 |
| **3N′** | 1/2 | (19,12) | $(\pi''_{nb})^2(\sigma_{nb})^2(\delta^*)^1(\pi'^*)^2(\pi''^*)^0(\sigma^*)^0$ | 71.5 |
| | | | $(\pi''_{nb})^0(\sigma_{nb})^2(\delta^*)^1(\pi'^*)^2(\pi''^*)^2(\sigma^*)^0$ | 14.9 |
| | | | $(\pi''_{nb})^1(\sigma_{nb})^2(\delta^*)^1(\pi'^*)^2(\pi''^*)^1(\sigma^*)^0$ | 3.21 |
| **3N′** | 3/2 | (19,12) | $(\pi''_{nb})^2(\sigma_{nb})^2(\delta^*)^1(\pi'^*)^1(\pi''^*)^1(\sigma^*)^0$ | 83.5 |

[a]CSFs = configuration state functions. All CSFs have six further doubly filled active orbitals, which are highly mixed.


DOI: 10.1021/jacs.5b12790
J. Am. Chem. Soc. 2016, 138, 2327−2341

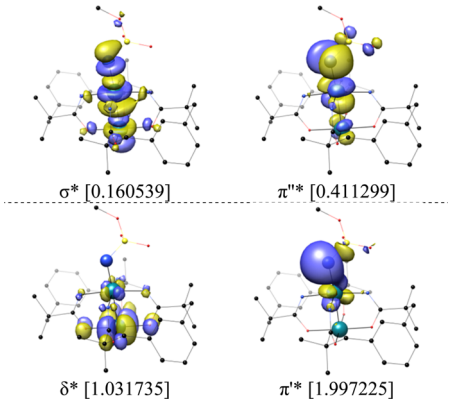


**Figure 5.** Natural frontier orbitals of doublet **3N′** from CASSCF. Occupation numbers are shown in brackets.

structure. We may describe the electronic structure as a resonance hybrid between a $(\delta^*)^2(\pi^{*\prime})^1(\pi^{*\prime\prime})^0$ configuration and an antiferromagnetic $(\delta^*)^d(\pi^{*\prime})^u(\pi^{*\prime\prime})^u$ configuration (here d and u denote spin-down and spin-up, respectively). The former configuration may be described in valence bond terms as having a $Rh_2$(II,II) unit with a coordinated nitrene radical cation, while the latter configuration indicates a $Rh_2$(II,III) species that is antiferromagnetically coupled to a triplet nitrene group. The view that both of these configurations contribute to the ground state is supported by the Mulliken spin populations showing very little (but negative) spin on the Rh centers and 1.05 spin on the nitrene N atom. It is remarkable that the calculations support partial oxidation of the nitrene moiety, itself a strong oxidant, by the $Rh_2(esp)_2^+$ core. This result is, however, in agreement with the high $Rh_2(esp)_2^{0/+}$ redox potential, but since we have shown the redox potentials to drop considerably upon chloride binding, it is likely that the electronic structure will change significantly as a function of the axial ligands.

As expected from the greater stabilization of higher oxidation states by espn, the major configuration of **3N′**, $(\delta^*)^1(\pi'^*)^2(\pi''^*)^0$, is best described as consisting of a $Rh_2$(II,III) unit coordinated by a singlet nitrene species (see the orbitals and occupation numbers given in Figure 5). Here, the spin population is clearly localized on the $Rh_2$ unit. In each case, there are other minor configurations contributing up to 26% of the wave function that are due to double and single excitations from the main configuration.

It is instructive at this juncture to compare the electronic structure of **2N′** and **3N′** to Co−porphyrin complexes, which have been shown to undergo metal-centered oxidation upon the binding of alkyl sulfamate nitrenes to give Co(III)(Por)-$(NSO_3R^{\bullet-})$ species.[70] As shown in Figure 6, the electronic structures of both **2N′** and **3N′** are quite different from that of the Co species. One reason for this difference can be understood from the redox potentials of the respective catalysts. **2** exhibits a $Rh_2^{4+/5+}$ couple at 0.78 V vs $Cp_2Fe$, and **3** exhibits a $Rh_2^{5+/6+}$ couple at 1.57 V vs $Cp_2Fe$ in $CH_2Cl_2$ (vide supra). In contrast, Co(TPP) (TPP = tetraphenylporphyrin) has been shown to exhibit three oxidation waves at 0.24, 0.45, and 0.61 V vs $Cp_2Fe$ in $CH_2Cl_2$, corresponding to one metal-centered and two ring-centered oxidations, respectively.[71] Thus, Co(II) is able to reduce the nitrene group to a radical anion while neither the $Rh_2(esp)_2^+$ core nor the $Rh_2(espn)_2^+$ core is reducing. In fact, $Rh_2(esp)_2^+$ is highly oxidizing, and there is a contribution to the GES of **2N′** from a $Rh_2$(II,II) species bearing a nitrene radical cation. In contrast, the $Rh_2(espn)_2^+$ core is content in the $Rh_2$(II,III) oxidation state and supports a bound singlet nitrene. In addition to the difference in the redox potentials, there is also a difference in the mechanism of C−H amination between the Co(Por) system, which has been proposed to proceed via a stepwise mechanism,[72] whereas we propose here that both $Rh_2$ systems operate via a concerted mechanism (vide infra).

We further investigated, at the DFT level, both doublet and quartet potential energy surfaces for C−H amination via the nitrene complexes $\{Rh_2(esp)_2(L)[NSO_3(CH_2)_3Ph]\}^{n+}$, **2N_L**, and $\{Rh_2(espn)_2(L)[NSO_3(CH_2)_3Ph]\}^{n+}$, **3N_L**, keeping in mind the caveat that the doublet states are multiconfigurational and that the DFT description of their electronic structure does not explicitly take this complexity into account. A full analysis of the potential energy surfaces at the CASSCF level cannot be performed because it is prohibitively expensive.

*2.2.2. Mechanistic Details of Intramolecular C−H Amination via **2N_L** and **3N_L** Nitrene Complexes.* There are two limiting mechanisms for nitrenoid C−H amination that should be considered: concerted (C) and stepwise (S) insertion of the

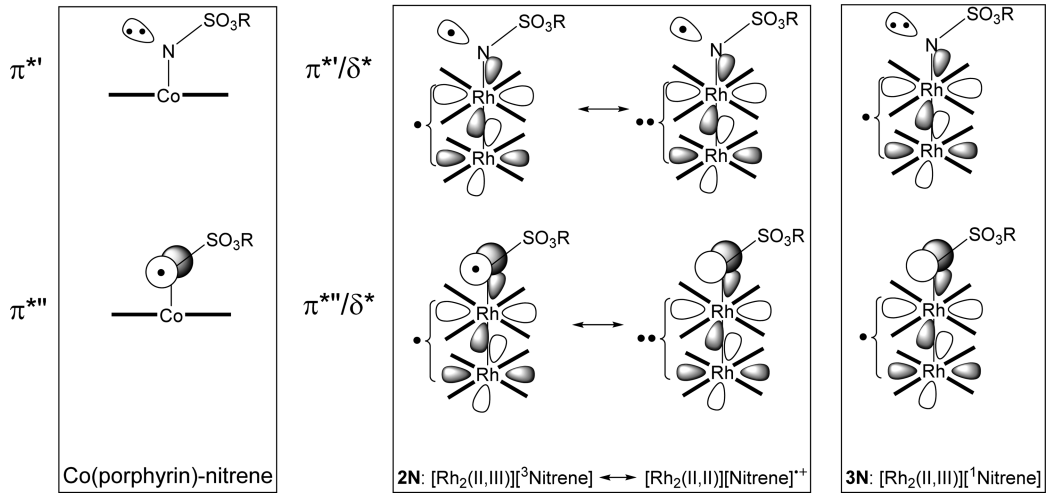


**Figure 6.** Comparison of the electronic structure of Co−porphyrin−nitrene(radical) species (left) with **2N′** (center) and **3N′** (right). Here, the two $\pi$-symmetry orbitals are shown separately and localized on N, and in the $Rh_2$ cases, the $\delta^*$ electrons are also shown.



DOI: 10.1021/jacs.5b12790
J. Am. Chem. Soc. 2016, 138, 2327−2341

nitrene into a substrate C−H bond (Scheme 4). In the C mechanism, there is a single transition state leading to $C^1$−N

**Scheme 4. Schematic Presentation of the Concerted (C) and Stepwise (S) Mechanisms of Intramolecular Nitrene Insertion into a Substrate C−H Bond in the 2N_L and 3N_L Nitrene Complexes**

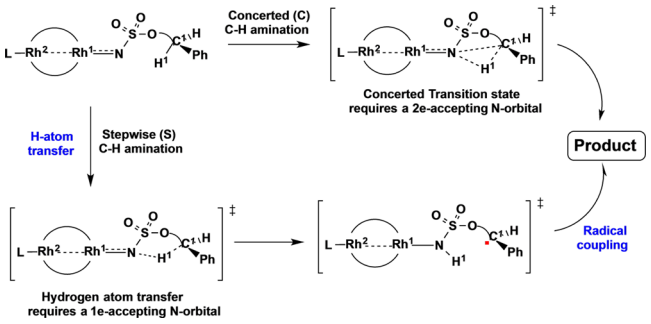


bond formation, $C^1$−$H^1$ bond cleavage, and N−$H^1$ bond formation. The S mechanism starts by hydrogen atom ($H^1$) transfer (HAT) to produce a protonated nitrene radical anion and a benzylic radical followed by radical recombination to yield the products. Unpaired spin density on the nitrene N atom is often naively suggested to support HAT in an S mechanism, but there are strong kinetic and thermodynamic arguments against such generalizations.[73] Below, we develop an electronic structure-based approach to understand the differences between a C and S mechanism.

If we consider the orbital requirements for a C mechanism, the three-membered N−$C^1$−$H^1$ ring of the transition state will require one orbital from each of the nuclei involved: a N p orbital (or $sp^x$ hybrid), a $C^1$ p- or $sp^x$-hybrid orbital, and a $H^1$ 1s orbital. The stabilization of a three-membered ring with three orbitals requires the presence of two electrons to form a 3c/2e bond. These two electrons obviously originate from the $C^1$−$H^1$ bond of the substrate. Thus, this mechanism requires an empty (but energetically accessible) N-centered orbital that can accept two electrons from the C−H bond.

The electronic requirements of the S mechanism are different. This mechanism relies on an HAT step and requires the N atom to accept a single electron. Therefore, this mechanism requires either an empty or half-filled N-centered orbital capable to accept the incoming $H^1$ atom with one unpaired electron.

Based on the aforementioned discussion, it can be expected that intramolecular C−H amination in the doublet state nitrene complexes with an empty and easily accessible Rh−Rh−N $\pi^*$ orbital will proceed via a C mechanism. On the other hand, the same process in the quartet state nitrene complexes, having two half-filled Rh−Rh−N $\pi^*$ orbitals, is expected to proceed via the S mechanism. Thus, the spin state of the nitrene intermediate is expected to play a significant role in determining the mechanism of C−H amination. This is not a consequence of differing spin population but orbital populations. Considering the electronic structure in Figure 6, one can easily see why the Co−porphyrins use an S mechanism.

Armed with the aforementioned electronic structure-based prediction of the reactivity of the **2N_L** and **3N_L** nitrene species, we set out to investigate the mechanisms (energy and geometries of all transition states, intermediates, and products) and controlling factors of intramolecular benzylic C−H bond

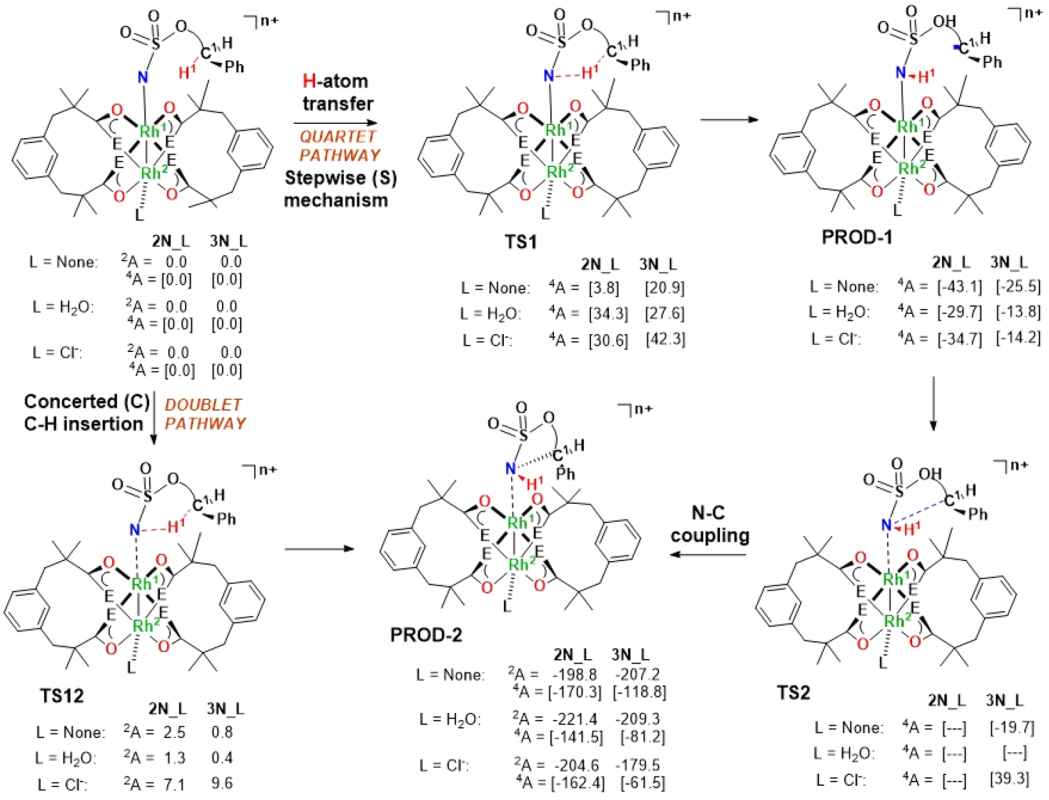


**Figure 7.** Schematic representation of the calculated reactants, intermediates, transition states, and products, alone with their relative energies (relative to the corresponding reactants, in kJ/mol), of the intramolecular C−H amination in the **2N_L** and **3N_L** nitrene complexes.



DOI: 10.1021/jacs.5b12790
J. Am. Chem. Soc. 2016, 138, 2327−2341

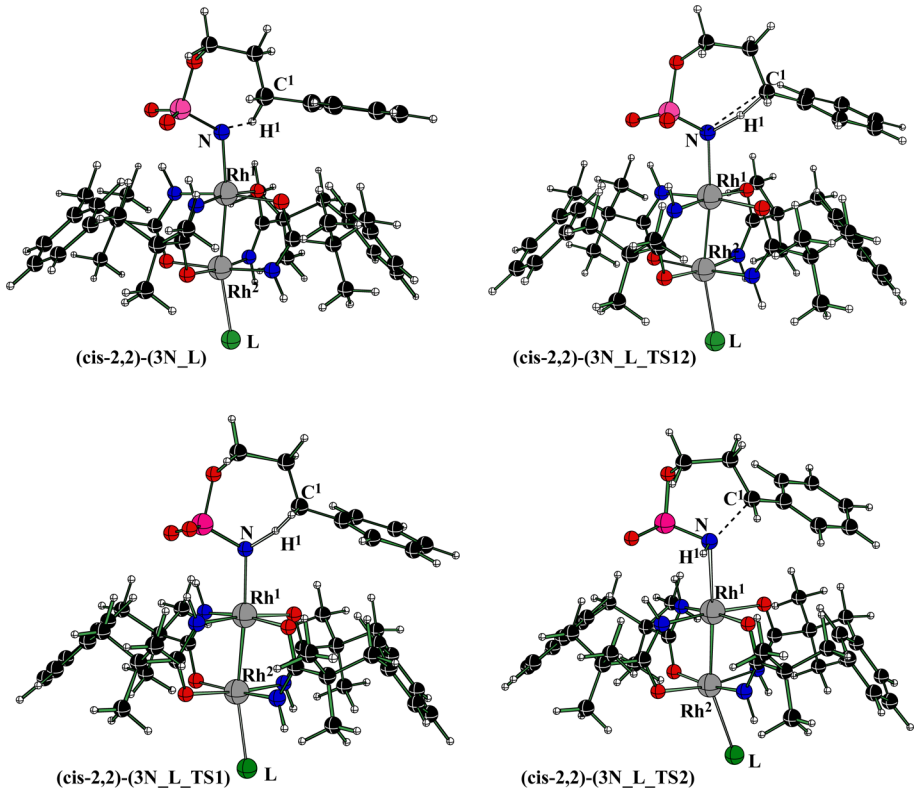


**Figure 8.** Calculated structures of the nitrene complex, and transition states **TS1**, **TS2**, and **TS12**. The structures of L = $Cl^-$ are shown here as an example. See Supporting Information for similar structures for other species.

amination in $NSO_3(CH_2)_3Ph$. Since the calculated energy difference between the doublet and quartet states of both starting **2N_L** and **3N_L** nitrene species is relatively small and is strongly dependent on the chemical compositions of these complexes, one may not clearly suggest which electronic state (doublet or quartet) of the **2N_L** and **3N_L** species is responsible in the amination reaction in experiments. In principle, depending on the concentrations of exogenous L ligands in solution, any of these electronic states of both **2N_L** and **3N_L** nitrene species could be a catalytically important one. Therefore, we studied the mechanisms of the intramolecular benzylic C−H bond amination with the $NSO_3(CH_2)_3Ph$ ligand for all these species at their lowest-energy doublet and quartet states. The calculated important intermediates, transition states, and products of these reactions with their relative free energies are given in Figure 7. Representative transition state structures are given in Figure 8. More details of all these structures are given in the Supporting Information.

*2.2.2.1. Intramolecular C−H Amination.* The exact mechanism of C−H amination is expected to depend strongly on the spin state of the nitrene reactant. As seen in Figure 7, all doublet nitrene species uniformly undergo nearly barrierless (0.4−9.6 kJ/mol, at the transition state **TS12**), concerted insertion of the nitrene into the $C^1$−$H^1$ bond. On the other hand, the quartet nitrene species undergo stepwise $C^1$−$H^1$ functionalization via a mechanism involving (1) $H^1$ atom abstraction with energy barriers of 3.8−42.3 kJ/mol, **TS1**, followed by (2) radical recombination, **TS2**. The recombination step is essentially barrierless for the **2N** species but for **3N** is uphill from the intermediate **PROD-1** by 5.8−53.5 kJ/mol, due to the different occupancies of the $\pi^*$ orbitals, depending strongly on the identity of L.

While it is tempting to assign the concerted pathway as the lowest-energy pathway and therefore the preferred pathway for catalysis, we must also keep in mind that in **3N_L** the quartet states are lower in energy and spin crossover to the doublet surface would be necessary in order to access the fastest rates of the doublet potential energy surface (see Scheme 5).[74,75] However, we should also consider that formation of **3N** is most likely to take place on a doublet surface ($^2Rh_2$(II,III) +

**Scheme 5. Simplified Reaction Coordinate Diagram for C−H Amination by $Rh_2$(II,III) Complexes**

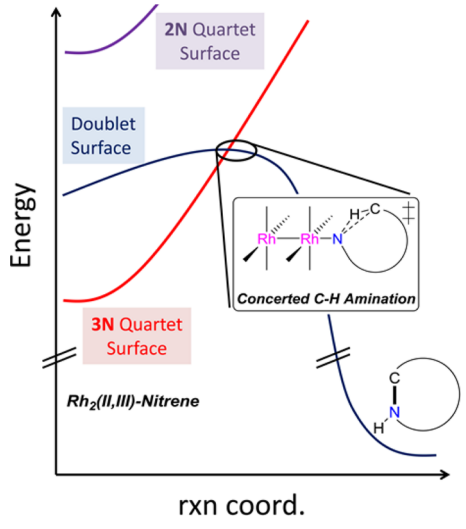



DOI: 10.1021/jacs.5b12790
J. Am. Chem. Soc. 2016, 138, 2327−2341

$^1$PhINSO$_3$R → $^2$**3N** + PhI). The main assumption underlying the proposed two-state reactivity for **3N** is that spin-state crossover is fast compared to the other barriers involved in nitrene formation and C−H amination. Under this assumption, the energy barriers are necessarily steeper for the **3N_L** compounds than their **2N_L** analogues since the former must undergo a spin-state change.

*2.2.2.2. Kinetic Isotope Effects.* One way to assess the computed reaction pathways is comparison of the predicted and measured kinetic isotope effect (KIE) of the reactions. We have experimentally determined the KIE under identical conditions for compounds **2** and **3** (see Chart 3), which are

**Chart 3. Reaction and Conditions for Experimental KIE Measurement**

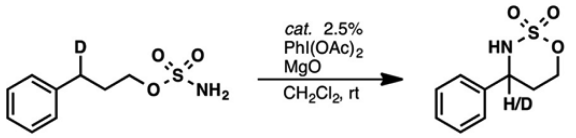


2.9 and 2.6, respectively. These are remarkably similar, especially considering that catalyst **2** is proposed to utilize both a Rh$_2$(II,III) and a Rh$_2$(II,II) mechanism. In comparison, the KIE for **1**, 1.9,[76] is somewhat smaller and may suggest that a Rh$_2$(II,III) pathway is not viable for **1**.[77] Undoubtedly, the KIE must be a product of all of the potential mechanisms and can even change over the course of a reaction if the nature of the active catalyst is changing, as is likely the case here. Given that KIEs of ∼2 are established for concerted nitrene transfer reactions, whereas values of ∼6 are associated with HAT steps, the experimental KIE values are more suggestive of a concerted intramolecular nitrene insertion mechanism.[78]

In agreement with this assessment, the calculated KIE values are 3.1, 2.3, and 2.8 for doublet state **2_N_L** with L = none, H$_2$O, and Cl$^-$, respectively, while the corresponding values for the quartet surface are 6.3, 6.1, and 5.9. For the **3_N_L** catalysts (L = none, H$_2$O, and Cl$^-$), the doublet KIEs are calculated to be 2.5, 1.8, and 2.1 and the quartet values are 5.9, 6.3, and 5.4. Thus, the calculated KIEs are significantly larger for the quartet state pathways than they are on the doublet state analogues. Moreover, the quartet values are too large compared to the experimental values. Thus, the doublet transition state appears to be the most important one for defining the C−H amination pathway despite the fact that the **3N_L** nitrene intermediates favor a quartet ground state. It is worth mentioning that since the exact identities of catalytic intermediates and active oxidant remain obscure at this time, we cannot hope to achieve better agreement between the experimental and computed KIEs.

## 3. CONCLUSIONS

From the above presented joint computational and experimental studies, we may draw the following conclusions.

(a) Rh$_2$(II,III) tetracarboxylate complexes, [Rh$_2^{II,III}$(O$_2$CCH$_3$)$_4$(L)$_n$]$^+$ (**1_L**) (L = none, Cl$^-$, and H$_2$O), have a $^2$E$_g$-derived ground electronic state with degenerate $\pi^*$ orbitals and a $(\pi^*)^3$ valence electronic configuration; therefore, the electronic structure of these compounds cannot be adequately modeled at the DFT level. CASSCF calculations of the EPR *g* values are in good agreement with their experimental values.

(b) Unlike typical Rh$_2$(II,III) tetracarboxylates, [Rh$_2$(esp)$_2$(L)$_n$]$^{m+}$, **2_(L)$_n$**, and [Rh$_2$(espn)$_2$(L)$_n$]$^{m+}$, **3_(L)$_n$** [where L = none with $m$ = 1, L = H$_2$O, $n$ = 1 or 2, with $m$ = 1, L = Cl$^-$, $n$ = 1, with $m$ = 0, and L = Cl$^-$, $n$ = 2, with $m$ = −1], species have a $^2$B$_{1u}$-derived ground electronic state with a $(\delta^*)^1$ valence electronic configuration, as evidenced by EPR spectroscopy and Cl K-edge XAS. Importantly, this state is not a multireference state and, therefore, can be modeled well using DFT methods.

(c) Nitrene complexes **2N_L** and **3N_L** of [Rh$_2$(esp)$_2$(L)$_n$]$^{m+}$, **2_(L)$_n$**, and [Rh$_2$(espn)$_2$(L)$_n$]$^{m+}$, **3_(L)$_n$**, respectively, are proposed to be reactive intermediates in C−H amination. For **2N**, a complex multideterminental doublet state is predicted to be lowest in energy, whereas **3N** favors a high-spin quartet ground electronic state with a $(\delta^*)^1(\pi^*)^2$ valence electronic configuration. Binding $\pi$-donor axial ligands destabilizes the quartet state.

(d) The calculated energy barriers for stepwise C−H amination in the quartet state are found to be uniformly higher than for concerted C−H amination in the doublet state. While **2N** is able to access the doublet surface directly, **3N** must undergo a change in spin state first, which leads in effect to higher barriers to C−H amination by the latter species. Thus, the gain in catalyst robustness in changing from carboxylate to amidate equatorial ligands is counterbalanced by a loss in catalyst efficiency.

(e) Experimental KIE measurements yield values that are too low to be in agreement with a stepwise, C−H abstraction/radical recombination pathway and show better agreement with the mechanism outlined in Scheme 5.

## 4. EXPERIMENTAL SECTION

**4.1. General Reagents and Methods.** Catalysts **1** and **2** were prepared by published methods.[6,40] All solvents were used as received without further purification unless otherwise noted. Electrochemical oxidation of **1** was performed according to a published protocol.[39]

**4.2. Electron Paramagnetic Resonance.** EPR data were acquired using a Varian Line X-band spectrometer equipped with a Varian E102 microwave bridge interfaced with a Linux system. An Oxford Instruments ESR-900 continuous-flow helium flow cryostat and an Oxford Instruments 3120 temperature controller were used to set and maintain the sample temperature. A Hewlett-Packard 432A power meter was used for microwave power calibration. Simulations were performed using EasySpin software.[79] The hyperfine fittings are based on line shape analysis.

**4.3. X-ray Absorption Spectroscopy.** Cl K-edge XAS spectra were measured at SSRL beamline 4-3 under ring conditions of 3 GeV and 500 mA. Samples were ground to a fine powder and were spread to a vanishing thickness onto 38 $\mu$m low-S Mylar tape. All samples were measured in a He atmosphere at room temperature in fluorescence mode using a Lytle detector. The incident beam energy was calibrated by setting the energy of the first inflection point in the Cl K-edge spectrum of KCl to 2824.8 eV. Intensity was normalized with respect to the incident beam using a He-filled ion chamber upstream of the sample. Data represent an average of six scans measured from 2720 to 3150 eV. Data were processed with SIXPACK. Spectra were normalized by fitting a polynomial flattened to energies below 2840 eV to the data and normalizing the region above this energy to unity.

**4.4. General Procedure for KIE Experiments.** 3-Phenylpropyl-3-D-sulfamate (105 mg, 0.48 mmol, 1.0 equiv) was combined with MgO (45 mg, 1.11 mmol, 2.3 equiv), dirhodium catalyst (12 mmol, 0.025 equiv), and 3.0 mL of CH$_2$Cl$_2$. The resulting suspension was stirred for 5 min, after which time PhI(OAc)$_2$ (172 mg, 0.534 mmol, 1.1 equiv) was added in a single portion. The reaction flask was sealed, and the mixture was stirred for 12 h. At the conclusion of this period,


DOI: 10.1021/jacs.5b12790
J. Am. Chem. Soc. 2016, 138, 2327−2341

the suspension was filtered through a short pad of Celite, and the flask and filter cake were rinsed with 5−10 mL of $CH_2Cl_2$. The filtrate was concentrated under reduced pressure to a purple oil. Purification of this material by chromatography on silica gel (20% EtOAc in hexanes) afforded the desired product mixture as a white solid. The kinetic isotope effect value was determined by $^{13}C$ NMR analysis using the method of Wang and Adams.[80]

**4.5. Computational Methods.** Calculations of g-tensors, redox potentials, and multiconfigurational electronic structures were performed using the ORCA software package version 3.0.3.[81] Potential energy surface calculations were performed by the Gaussian_09 suite of programs.[82] Orbitals were visualized using the MOLEKEL software program[83] or UCSF chimera software program.[84]

**4.6. Calculation of EPR g-Tensors of 1_L and 2_L.** EPR g-tensors of **1_L** and $[trans\text{-}Rh_2(esp)_2]^+$ were calculated on top of DFT-optimized geometry according to the method described above. For **1_Cl2**, the geometry was obtained from the reported crystal structure of $((NH_2)_3C)_2[Rh_2(OAc)_4Cl_2]$ without further optimization. To calculate the g-tensors for all the complexes studied, the B3LYP functional with scalar relativistically recontracted basis set of TZVP (SARC-TZVP)[85,86] was used. Scalar relativistic effects were accounted for in the Hamiltonian by the zeroth-order regular approximation (ZORA) using the model potential of van Wullen.[87]

Ab initio multireference configuration interaction (MRCI) calculations of the molecular g-tensors for dirhodium tetra-acetate complexes were performed on top of DFT-optimized geometries, except for $[Rh_2(OAc)_4Cl_2]^-$ (vide infra). The DFT geometries were optimized using the BP86[88,89] functional with the SARC-def2-TZVPP basis set on Rh and the SARC-def2-SVP basis set on the rest of the atoms. Scalar relativistic effects were accounted for by ZORA. The evaluation of the Coulomb integrals were approximated by the resolution of identity (RI) approach.[90] Dispersion effects were treated with the D3[91] correction. The MRCI calculations were performed at the state-averaged complete active space self-consistent field (SA-CASSCF)[92] wave functions. Here, the MRCI approach was modeled by the multireference difference-dedicated configuration interaction theory with two degrees of freedom (MR-DDCI2).[93,94] To calculate the molecular g-tensors, first-order perturbation on the converged MRDDCI2:CASSCF wave function using the electronic Zeeman Hamiltonian was performed. The effect of spin−orbit coupling was introduced using the quasi-degenerate perturbation theory,[95,96] with the spin−orbit mean-field Hamiltonian. In the SA-CASSCF calculations, we used different active spaces to incorporate the effects of axial ligands. An active space of 13 electrons in eight orbitals (13,8) was used for the axially free $[Rh_2(OAc)_4]^+$ complex to include all metal d orbitals except the two $d_{x^2-y^2}$ orbitals which are highly antibonding with respect to the equatorial ligands. An active space of (17,10), which includes all spin−orbitals in (13,8) and four electrons in two $\sigma$ orbitals from both $H_2O$ ligands, was used for the bis(aquo) complex. An active space of (19,11), which includes all spin−orbitals in (13,8) and six electrons in three orbitals from the 3p orbitals of $Cl^-$, was used for the chloro complex. An active space of 25 electrons in 14 orbitals (25,14), which includes all spin−orbitals in (13,8) and 12 electrons in six orbitals from the 3p orbitals of both $Cl^-$, was used for the dichloro complex.

CASSCF calculations on the nitrene complexes, **2N** and **3N**, were performed on truncated models, denoting **2N′** and **3N′**, with the organic substituent on the nitrene replaced by a methyl group. A (19,12) active space was used. This active space includes (13,8) from both rhodium atoms and (7,4) from the nitrene, which are N 2s orbital and nitrene one $\sigma$ and two $\pi$ orbitals. The inclusion of the N 2s orbital helps stabilize the convergence of the CASSCF calculations.

**4.7. Calculation of the Redox Potentials of 2_L and 3_L.** DFT prediction of redox potentials was performed using a slightly modified procedure following an established method.[56] Geometries were optimized in gas phase followed by single-point energy calculations in $CH_2Cl_2$. Solvation were modeled by conductor-like screening model (COSMO). The Gibbs free energies of the redox half reaction in $CH_2Cl_2$ were calculated as follows:

$$\Delta G_{solv}^{abs,redox} = \Delta G_{g}^{abs,redox} + \Delta G_{s}^{o}(Red)$$

and the calculated Gibbs free energies were converted to absolute electron redox potential according to the Nernst equation:

$$\Delta G_{solv}^{abs,redox} = -FE_{calc}^{abs}$$

where $F$ is the Faraday constant, 96 500 C $mol^{-1}$. The calculated absolute redox potentials of the half-reaction were converted to standard potentials:

$$E_{calc}^{o} = E_{calc}^{abs} + E^{abs}(H_2/H^+)$$

where $E_{calc}^{abs}(H_2/H^+)$ is a literature value of −4.44 V.[97] The calculated standard potentials were converted to referenced potentials (vs $Fc/Fc^+$):

$$E_{calc}^{Fc} = E_{calc}^{o} - E^{o}(Fc/Fc^+)$$

where $E^o(Fc/Fc^+)$ is 0.46 V.[98]

**4.8. Calculation of the C−H Amination by 2N_L and 3N_L.** Studies of potential energy surfaces of the C−H amination in **2N_L** and **3N_L** complexes used the M06L density functional[99] in conjunction with the 6-31G** basis sets for C, H, N, O, and S atoms[100] and LANL08(f) basis sets (with their corresponding ECPs) for Rh atoms (referred to below as basis sets BS1).[101−103] All reported structures were fully optimized without any geometry constraints. Previously, it was reported that this computational method describes the energies and geometries of organometallic compounds well.[64−67] Frequency calculations were carried out to verify the nature of the located stationary points. Graphical analysis of the imaginary vibrational normal modes as well as the performed IRC calculations confirmed the nature of the located transition states. Energetics of the reported structures were improved by performing single-point energy calculations at the M06L level of theory in conjunction with the 6-311+G(df,p) basis sets for C, H, O, N, and S atoms[100] and LANL08(f) for the Rh centers (referred to below as basis sets BS2). In these calculations, we used the M06L/BS1 optimized geometries. The reported thermodynamic data were computed at 298.15 K and 1 atm pressure. Solvent effects in dichloromethane were included by means of the PCM method.[104] In these calculations, the free energy of solvation was computed as

$$\Delta\Delta G_{solv} = G_{solv,PCM} - E_{el}$$

where the final free energy in solution is obtained as

$$G_{solv} = G_{gas} + \Delta\Delta G_{solv}$$

## ■ ASSOCIATED CONTENT

### Supporting Information

The Supporting Information is available free of charge on the ACS Publications website at DOI: 10.1021/jacs.5b12790.

Figures S1 and S2 and Tables S1−S3 (PDF)

## ■ AUTHOR INFORMATION


### Corresponding Authors

*berry@chem.wisc.edu

*dmusaev@emory.edu

### Author Contributions

⊥A.V.-A. and T.Y. contributed equally to this work.


### Notes

The authors declare no competing financial interest.

## ■ ACKNOWLEDGMENTS

We thank the Center for Selective C−H Functionalization supported by the National Science Foundation (CHE-1205646). J.F.B. additionally thanks the DOE (DE-FG02-10ER16204). K.M.L. acknowledges NSF CHE-1454455 for



DOI: 10.1021/jacs.5b12790
J. Am. Chem. Soc. 2016, 138, 2327−2341

support. The authors gratefully acknowledge NSF MRI-R2 grant (CHE-0958205) and the use of the resources of the Cherry Emerson Center for Scientific Computation. The computational and EPR facilities at UW—Madison are supported by grants from the National Science Foundation (CHE-0840494 and CHE-0741901, respectively). The UCSF Chimera package is developed by the Resource for Biocomputing, Visualization, and Informatics at the University of California, San Francisco (supported by NIGMS P41-GM103311). We acknowledge the UW-Madison Center For High Throughput Computing (CHTC) in the Department of Computer Sciences. The CHTC is supported by UW-Madison, the Advanced Computing Initiative, the Wisconsin Alumni Research Foundation, the Wisconsin Institutes for Discovery, and the National Science Foundation, and is an active member of the Open Science Grid, supported by the National Science Foundation and the U.S. Department of Energy Office of Science.

## REFERENCES

(1) Davies, H. M. L.; Manning, J. R. *Nature* **2008**, *451*, 417−424.
(2) Zalatan, D. N.; Du Bois, J. In *Topics in Current Chemistry*; Yu, J.-Q., Shi, Z., Eds.; Springer-Verlag: Berlin, 2010; Vol. *292*, pp 347−378.
(3) Du Bois, J. *Org. Process Res. Dev.* **2011**, *15*, 758−762.
(4) Roizen, J. L.; Harvey, M. E.; Du Bois, J. *Acc. Chem. Res.* **2012**, *45*, 911−922.
(5) Kornecki, K. P.; Berry, J. F.; Powers, D. C.; Ritter, T. In *Progress in Inorganic Chemistry*; Karlin, K. D., Ed.; Wiley: New York, 2014; Vol. *58*, pp 225−302. DOI: 10.1002/9781118792797.ch04.
(6) Espino, C. G.; Fiori, K. W.; Kim, M.; Du Bois, J. *J. Am. Chem. Soc.* **2004**, *126*, 15378−15379.
(7) Cui, Y.; He, C. *Angew. Chem., Int. Ed.* **2004**, *43*, 4210−4212.
(8) Li, Z. G.; Capretto, D. A.; Rahaman, R.; He, C. A. *Angew. Chem., Int. Ed.* **2007**, *46*, 5184−5186.
(9) Beltran, A.; Lescot, C.; Diaz-Requejo, M. M.; Perez, P. J.; Dauban, P. *Tetrahedron* **2013**, *69*, 4488−4492.
(10) Rigoli, J. W.; Weatherly, C. D.; Alderson, J. M.; Vo, B. T.; Schomaker, J. M. *J. Am. Chem. Soc.* **2013**, *135*, 17238−17241.
(11) Scamp, R. J.; Rigoli, J. W.; Schomaker, J. M. *Pure Appl. Chem.* **2014**, *86*, 381−393.
(12) Breslow, R.; Gellman, S. H. *J. Am. Chem. Soc.* **1983**, *105*, 6728−6729.
(13) Mahy, J. P.; Bedi, G.; Battioni, P.; Mansuy, D. *New J. Chem.* **1989**, *13*, 651−657.
(14) Liu, Y. G.; Che, C. M. *Chem. - Eur. J.* **2010**, *16*, 10494−10501.
(15) Liu, Y. G.; Wei, J. H.; Che, C. M. *Chem. Commun.* **2010**, *46*, 6926−6928.
(16) Paradine, S. M.; White, M. C. *J. Am. Chem. Soc.* **2012**, *134*, 2036−2039.
(17) Liu, Y. G.; Guan, X. G.; Wong, E. L. M.; Liu, P.; Huang, J. S.; Che, C. M. *J. Am. Chem. Soc.* **2013**, *135*, 7194−7204.
(18) Wang, H. Y.; Li, Y. X.; Wang, Z. M.; Lou, J.; Xiao, Y. L.; Qiu, G. F.; Hu, X. M.; Altenbach, H. J.; Liu, P. *RSC Adv.* **2014**, *4*, 25287−25290.
(19) Yu, X. Q.; Huang, J. S.; Zhou, X. G.; Che, C. M. *Org. Lett.* **2000**, *2*, 2233−2236.
(20) Paradine, S. M.; Griffin, J. R.; Zhao, J. P.; Petronico, A. L.; Miller, S. M.; White, M. C. *Nat. Chem.* **2015**, *7*, 987−994.
(21) Liang, J. L.; Yuan, S. X.; Huang, J. S.; Che, C. M. *J. Org. Chem.* **2004**, *69*, 3610−3619.
(22) Milczek, E.; Boudet, N.; Blakey, S. *Angew. Chem., Int. Ed.* **2008**, *47*, 6825−6828.
(23) Au, S. M.; Huang, J. S.; Yu, W. Y.; Fung, W. H.; Che, C. M. *J. Am. Chem. Soc.* **1999**, *121*, 9120−9132.
(24) Díaz-Requejo, M. M.; Belderraín, T. R.; Nicasio, M. C.; Trofimenko, S.; Pérez, P. J. *J. Am. Chem. Soc.* **2003**, *125*, 12078−12079.
(25) Pelletier, G.; Powell, D. A. *Org. Lett.* **2006**, *8*, 6031−6034.
(26) Powell, D. A.; Fan, H. *J. Org. Chem.* **2010**, *75*, 2726−2729.
(27) Gephart, R. T.; Warren, T. H. *Organometallics* **2012**, *31*, 7728−7752.
(28) Bagchi, V.; Paraskevopoulou, P.; Das, P.; Chi, L. Y.; Wang, Q. W.; Choudhury, A.; Mathieson, J. S.; Cronin, L.; Pardue, D. B.; Cundari, T. R.; Mitrikas, G.; Sanakis, Y.; Stavropoulos, P. *J. Am. Chem. Soc.* **2014**, *136*, 11362−11381.
(29) Caballero, A.; Díaz-Requejo, M. M.; Belderraín, T. R.; Nicasio, M. C.; Trofimenko, S.; Pérez, P. J. *J. Am. Chem. Soc.* **2003**, *125*, 1446−1447.
(30) Fructos, M. R.; Trofimenko, S.; Díaz-Requejo, M. M.; Pérez, P. J. *J. Am. Chem. Soc.* **2006**, *128*, 11784−11791.
(31) Huang, G. H.; Li, J. M.; Huang, J. J.; Lin, J. D.; Chuang, G. J. *Chem. - Eur. J.* **2014**, *20*, 5240−5243.
(32) Cui, X.; Xu, X.; Jin, L. M.; Wojtas, L.; Zhang, X. P. *Chem. Sci.* **2015**, *6*, 1219−1224.
(33) Lu, H. J.; Li, C. Q.; Jiang, H. L.; Lizardi, C. L.; Zhang, X. P. *Angew. Chem., Int. Ed.* **2014**, *53*, 7028−7032.
(34) Lu, H. J.; Hu, Y.; Jiang, H. L.; Wojtas, L.; Zhang, X. P. *Org. Lett.* **2012**, *14*, 5158−5161.
(35) Fiori, K. W.; Du Bois, J. *J. Am. Chem. Soc.* **2007**, *129*, 562−568.
(36) Davies, H. M. L.; Morton, D. *Chem. Soc. Rev.* **2011**, *40*, 1857−1869.
(37) Zalatan, D. N.; Du Bois, J. *J. Am. Chem. Soc.* **2009**, *131*, 7558−7559.
(38) Perry, R. H.; Cahill, T. J., III; Roizen, J. L.; Du Bois, J.; Zare, R. N. *Proc. Natl. Acad. Sci. U. S. A.* **2012**, *109*, 18295−18299.
(39) Kornecki, K. P.; Berry, J. F. *Chem. - Eur. J.* **2011**, *17*, 5827−5832.
(40) Kornecki, K. P.; Berry, J. F. *Chem. Commun.* **2012**, *48*, 12097−12099.
(41) Doyle, M. P. *J. Org. Chem.* **2006**, *71*, 9253−9260.
(42) Norman, J. G.; Renzoni, G. E.; Case, D. A. *J. Am. Chem. Soc.* **1979**, *101*, 5256−5267.
(43) Cotton, F. A.; Murillo, C. A.; Walton, R. A. In *Multiple Bonds Between Metal Atoms*, 3rd ed.; Springer Science and Business Media, Inc.: New York, 2005.
(44) Lichtenberger, D. L.; Pollard, J. R.; Lynn, M. A.; Cotton, F. A.; Feng, X. J. *J. Am. Chem. Soc.* **2000**, *122*, 3182−3190.
(45) McNaughton, R. L.; Roemelt, M.; Chin, J. M.; Schrock, R. R.; Neese, F.; Hoffman, B. M. *J. Am. Chem. Soc.* **2010**, *132*, 8645−8656.
(46) Kawamura, T.; Fukamachi, K.; Sowa, T.; Hayashida, S.; Yonezawa, T. *J. Am. Chem. Soc.* **1981**, *103*, 364−369.
(47) Kawamura, T.; Katayama, H.; Yamabe, T. *Chem. Phys. Lett.* **1986**, *130*, 20−23.
(48) Kawamura, T.; Katayama, H.; Nishikawa, H.; Yamabe, T. *J. Am. Chem. Soc.* **1989**, *111*, 8156−8160.
(49) Kawamura, T.; Maeda, M.; Miyamoto, M.; Usami, H.; Imaeda, K.; Ebihara, M. *J. Am. Chem. Soc.* **1998**, *120*, 8136−8142.
(50) Chavan, M. Y.; Zhu, T. P.; Lin, X. Q.; Ahsan, M. Q.; Bear, J. L.; Kadish, K. M. *Inorg. Chem.* **1984**, *23*, 4538−4545.
(51) Schafer, A.; Horn, H.; Ahlrichs, R. *J. Chem. Phys.* **1992**, *97*, 2571−2577.
(52) Vosko, S. H.; Wilk, L.; Nusair, M. *Can. J. Phys.* **1980**, *58*, 1200−1211.
(53) Lee, C. T.; Yang, W. T.; Parr, R. G. *Phys. Rev. B: Condens. Matter Mater. Phys.* **1988**, *37*, 785−789.
(54) Becke, A. D. *J. Chem. Phys.* **1993**, *98*, 1372−1377.
(55) Stephens, P. J.; Devlin, F. J.; Chabalowski, C. F.; Frisch, M. J. *J. Phys. Chem.* **1994**, *98*, 11623−11627.
(56) Roy, L. E.; Jakubikova, E.; Guthrie, M. G.; Batista, E. R. *J. Phys. Chem. A* **2009**, *113*, 6745−6750.
(57) For **1**, a $^2B_{1u}$ state was initially obtained, but the ∼8 kJ/mol lower energy $^2E_g$ state could be converged by rotation of the orbitals.
(58) Bersuker, I. B. *J. Comput. Chem.* **1997**, *18*, 260−267.
(59) Warzecha, E.; Berto, T. C.; Berry, J. F. *Inorg. Chem.* **2015**, *54*, 8817−8824.
(60) Berry, J. F. *Dalton Trans.* **2012**, *41*, 700−713.


DOI: 10.1021/jacs.5b12790
*J. Am. Chem. Soc.* 2016, 138, 2327−2341

(61) Kornecki, K. P.; Briones, J. F.; Boyarskikh, V.; Fullilove, F.; Autschbach, J.; Schrote, K. E.; Lancaster, K. M.; Davies, H. M. L.; Berry, J. F. *Science* **2013**, *342*, 351−354.
(62) Pap, J. S.; George, S. D.; Berry, J. F. *Angew. Chem., Int. Ed.* **2008**, *47*, 10102−10105.
(63) Sperger, T.; Sanhueza, I. A.; Kalvet, I.; Schoenebeck, F. *Chem. Rev.* **2015**, *115*, 9532−9586.
(64) Harvey, M. E.; Musaev, D. G.; Du Bois, J. *J. Am. Chem. Soc.* **2011**, *133*, 17207−17216.
(65) Qin, C.; Boyarskikh, V.; Hansen, J. H.; Hardcastle, K. I.; Musaev, D. G.; Davies, H. M. L. *J. Am. Chem. Soc.* **2011**, *133*, 19198−19204.
(66) Li, Z.; Boyarskikh, V.; Hansen, J. H.; Autschbach, J.; Musaev, D. G.; Davies, H. M. L. *J. Am. Chem. Soc.* **2012**, *134*, 15497−15504.
(67) Wang, H.; Guptill, D. M.; Varela-Álvarez, A.; Musaev, D. G.; Davies, H. M. L. *Chem. Sci.* **2013**, *4*, 2844−2850.
(68) Berry, J. F. *Comments Inorg. Chem.* **2009**, *30*, 28−66.
(69) Brown, T. R.; Dolinar, B. S.; Hillard, E. A.; Clérac, R.; Berry, J. F. *Inorg. Chem.* **2015**, *54*, 8571−8589.
(70) Goswami, M.; Lyaskovskyy, V.; Domingos, S. R.; Buma, W. J.; Woutersen, S.; Troeppner, O.; Ivanovic-Burmazovic, I.; Lu, H. J.; Cui, X.; Zhang, X. P.; Reijerse, E. J.; DeBeer, S.; van Schooneveld, M. M.; Pfaff, F. F.; Ray, K.; de Bruin, B. *J. Am. Chem. Soc.* **2015**, *137*, 5468−5479.
(71) Truxillo, L. A.; Davis, D. G. *Anal. Chem.* **1975**, *47*, 2260−2267.
(72) Lyaskovskyy, V.; Suarez, A. I. O.; Lu, H. J.; Jiang, H. L.; Zhang, X. P.; de Bruin, B. *J. Am. Chem. Soc.* **2011**, *133*, 12264−12273.
(73) Saouma, C. T.; Mayer, J. M. *Chem. Sci.* **2014**, *5*, 21−31.
(74) Schroder, D.; Shaik, S.; Schwarz, H. *Acc. Chem. Res.* **2000**, *33*, 139−145.
(75) Harvey, J. N.; Poli, R.; Smith, K. M. *Coord. Chem. Rev.* **2003**, *238*, 347−361.
(76) Fiori, K. W.; Espino, C. G.; Brodsky, B. H.; Du Bois, J. *Tetrahedron* **2009**, *65*, 3042−3051.
(77) We note that this KIE increases to 2.6 when one uses a longer delay time on the $^{13}$C NMR acquisition, as described in ref 64. Thus, we cannot completely rule out a $Rh_2$(II,III) pathway for $Rh_2(OAc)_4$.
(78) Collet, F.; Lescot, C.; Liang, C.; Dauban, P. *Dalton Trans.* **2010**, *39*, 10401−10413.
(79) Stoll, S.; Schweiger, A. *J. Magn. Reson.* **2006**, *178*, 42−55.
(80) Wang, P.; Adams, J. *J. Am. Chem. Soc.* **1994**, *116*, 3296−3305.
(81) Neese, F. *Wiley Interdisciplinary Reviews-Computational Molecular Science* **2012**, *2*, 73−78.
(82) Frisch, M. J.; Trucks, G. W.; Schlegel, H. B.; Scuseria, G. E.; Robb, M. A.; Cheeseman, J. R.; Scalmani, G.; Barone, V.; Mennucci, B.; Petersson, G. A.; Nakatsuji, H.; Caricato, M.; Li, X.; Hratchian, H. P.; Izmaylov, A. F.; Bloino, J.; Zheng, G.; Sonnenberg, J. L.; Hada, M.; Ehara, M.; Toyota, K.; Fukuda, R.; Hasegawa, J.; Ishida, M.; Nakajima, T.; Honda, Y.; Kitao, O.; Nakai, H.; Vreven, T.; Montgomery, J. A., Jr.; Peralta, J. E.; Ogliaro, F.; Bearpark, M.; Heyd, J. J.; Brothers, E.; Kudin, K. N.; Staroverov, V. N.; Kobayashi, R.; Normand, J.; Raghavachari, K.; Rendell, A.; Burant, J. C.; Iyengar, S. S.; Tomasi, J.; Cossi, M.; Rega, N.; Millam, J. M.; Klene, M.; Knox, J. E.; Cross, J. B.; Bakken, V.; Adamo, C.; Jaramillo, J.; Gomperts, R.; Stratmann, R. E.; Yazyev, O.; Austin, A. J.; Cammi, R.; Pomelli, C.; Ochterski, J. W.; Martin, R. L.; Morokuma, K.; Zakrzewski, V. G.; Voth, G. A.; Salvador, P.; Dannenberg, J. J.; Dapprich, S.; Daniels, A. D.; Farkas, Ö.; Foresman, J. B.; Ortiz, J. V.; Cioslowski, J.; Fox, D. J. *Gaussian 09*, revision D01; Gaussian, Inc.: Wallingford, CT, 2009.
(83) Flükiger, P.; Lüthi, H. P.; Portmann, S.; Weber, J. *MOLEKEL*, 4.0; Swiss Center for Scientific Computing: Manno, Switzerland, 2000.
(84) Pettersen, E. F.; Goddard, T. D.; Huang, C. C.; Couch, G. S.; Greenblatt, D. M.; Meng, E. C.; Ferrin, T. E. *J. Comput. Chem.* **2004**, *25*, 1605−1612.
(85) Pantazis, D. A.; Chen, X.-Y.; Landis, C. R.; Neese, F. *J. Chem. Theory Comput.* **2008**, *4*, 908−919.
(86) Weigend, F.; Ahlrichs, R. *Phys. Chem. Chem. Phys.* **2005**, *7*, 3297−3305.
(87) van Wullen, C. *J. Chem. Phys.* **1998**, *109*, 392−399.
(88) Perdew, J. P. *Phys. Rev. B: Condens. Matter Mater. Phys.* **1986**, *33*, 8822−8824.
(89) Becke, A. D. *Phys. Rev. A: At., Mol., Opt. Phys.* **1988**, *38*, 3098−3100.
(90) Weigend, F. *Phys. Chem. Chem. Phys.* **2006**, *8*, 1057−1065.
(91) Grimme, S.; Antony, J.; Ehrlich, S.; Krieg, H. *J. Chem. Phys.* **2010**, *132*, 154104.
(92) Roos, B. O.; Taylor, P. R.; Siegbahn, P. E. M. *Chem. Phys.* **1980**, *48*, 157−173.
(93) Miralles, J.; Daudey, J. P.; Caballol, R. *Chem. Phys. Lett.* **1992**, *198*, 555−562.
(94) Miralles, J.; Castell, O.; Caballol, R.; Malrieu, J. P. *Chem. Phys.* **1993**, *172*, 33−43.
(95) Ganyushin, D.; Neese, F. *J. Chem. Phys.* **2006**, *125*, 24103.
(96) Neese, F.; Petrenko, T.; Ganyushin, D.; Olbrich, G. *Coord. Chem. Rev.* **2007**, *251*, 288−327.
(97) Trasatti, S. *Pure Appl. Chem.* **1986**, *58*, 955−966.
(98) Connelly, N. G.; Geiger, W. E. *Chem. Rev.* **1996**, *96*, 877−910.
(99) Zhao, Y.; Truhlar, D. G. *J. Chem. Phys.* **2006**, *125*, 194101.
(100) Hehre, W. J.; Radom, L.; Schleyer, P. v. R.; Pople, J. A. *Ab Initio Molecular Orbital Theory*; John Wiley & Sons: New York, 1986.
(101) Hay, P. J.; Wadt, W. R. *J. Chem. Phys.* **1985**, *82*, 299−310.
(102) Roy, L. E.; Hay, P. J.; Martin, R. L. *J. Chem. Theory Comput.* **2008**, *4*, 1029−1031.
(103) Ehlers, A. W.; Bohme, M.; Dapprich, S.; Gobbi, A.; Hollwarth, A.; Jonas, V.; Kohler, K. F.; Stegmann, R.; Veldkamp, A.; Frenking, G. *Chem. Phys. Lett.* **1993**, *208*, 111−114.
(104) Tomasi, J.; Mennucci, B.; Cammi, R. *Chem. Rev.* **2005**, *105*, 2999−3093.
(105) Miskowski, V. M.; Dallinger, R. F.; Christoph, G. G.; Morris, D. E.; Spies, G. H.; Woodruff, W. H. *Inorg. Chem.* **1987**, *26*, 2127−2132.


DOI: 10.1021/jacs.5b12790
*J. Am. Chem. Soc.* 2016, 138, 2327−2341